

# Numerical Assessment for Accuracy and Efficiency of Time Evolution Schemes in TD-DMRG algorithm: CPU vs GPU

Weitang Li, Jiajun Ren,<sup>\*</sup> and Zhigang Shuai

*MOE Key Laboratory of Organic OptoElectronics and Molecular Engineering, Department of Chemistry, Tsinghua University, Beijing 100084, People's Republic of China*

E-mail: renjj@mail.tsinghua.edu.cn

## Abstract

Time dependent density matrix renormalization group (TD-DMRG) has become one of the cutting edge methods of quantum dynamics for complex systems. In this paper, we comparatively study the accuracy and efficiency for three time evolution schemes in TD-DMRG method, the direct propagation and compression with 4th order Runge-Kutta propagator (P&C-RK4), time dependent variational principle with matrix unfolding (TDVP-MU) and projector splitting (PS) by performing benchmarks on the exciton dynamics of Fenna-Matthews-Olson (FMO) complex. We show that the PS scheme is the most accurate and the fastest method because the propagation in each step is unitary by combining Krylov subspace algorithm and there is no error caused by regularization or instability of matrix inversion. We also compare the parallelization efficiency of multi-core central processing units (CPU) with graphical processing units (GPU) and we find that although 28 cores of CPU can merely double the speed, GPU is able to speedup the TDVP-MU and PS scheme by up to 57 times through efficient acceleration of matrix multiplication. Using the optimal strategy, we are able to simulate

the full quantum exciton dynamics of 7-site FMO model with 252 degrees of freedom to a timescale of 1 ps at fairly high accuracy within only 4 minutes.

# 1 Introduction

Time dependent density matrix renormalization group (TD-DMRG) has emerged as a powerful tool to deal with many-body chemical and physical problems.<sup>1,2</sup> Although DMRG is initially designed to solve the ground state of one dimensional strongly correlated systems,<sup>3,4</sup> its applications are successfully extended to dynamical properties both in the time and frequency domains, such as linear and nonlinear optical response of polyenes,<sup>5</sup> polaron formation and diffusion,<sup>6-8</sup> interconversion dynamics of pyrazine,<sup>9,10</sup> ab initio electronic dynamics in hydrogen chain,<sup>11</sup> exciton dissociation,<sup>12</sup> spectra of molecular aggregates<sup>13</sup> and many other topics.<sup>14-19</sup> One of the key components in TD-DMRG is the time evolution scheme, which is essential to the numerical accuracy and efficiency. The available schemes could be roughly classified into three groups. The first group is based on globally approximating the formal propagator  $e^{-iHt}$  or the outcome  $e^{-iHt} |\Psi\rangle$ , including time-evolving block decimation (TEBD),<sup>20-22</sup>  $W^{I,II}$  method,<sup>23</sup> Runge-Kutta,<sup>13,24</sup> Chebyshev expansion,<sup>25</sup> Krylov subspace<sup>24,26</sup> and split operator on the grid basis.<sup>9</sup> The same feature shared in these schemes is that in each time step the wavefunction is firstly propagated (P) as a whole globally and then compressed (C). Hence we call them P&C scheme. The second group is more inspired by the original DMRG, which is formulated in the local renormalized space. The representatives are time step targeting method (TST)<sup>27</sup> and some related variants.<sup>11,28</sup> The third group is based on the time dependent variational principle (TDVP).<sup>29,30</sup> Depending on the different ways to derive the equations of motion (EOMs), this group includes original TDVP-EOM method with fixed gauge freedom<sup>31</sup> and the more recent projector splitting method (PS) from a tangent space view.<sup>32</sup> It is worth mentioning that TD-DMRG with this group of evolution schemes shares a lot of similarities with multi-layer multi-configuration time-dependent

Hartree (ML-MCTDH).<sup>33,34</sup> In fact, the original TDVP-EOM method is the standard evolution scheme in MCTDH all the time<sup>33-35</sup> and PS has also been explored recently.<sup>36,37</sup> Among the above evolution schemes, all schemes are suited to long-range interactions except TEBD. In addition, the P&C scheme is the most simple and intuitive one and allows the adaptive growth of bond dimension during the time evolution, while the PS scheme seems to have become the most popular choice for systems with long-range interactions as it has been widely employed in the recent articles<sup>10,16-18,38</sup> and implemented in a number of TD-DMRG packages.<sup>39,40</sup> Although many evolution algorithms have been applied extensively to the calculation of chemical and physical dynamics, a pragmatic analysis of their relative accuracy and efficiency has not been reported yet.

In the past decade, the application of graphical processing units (GPUs) in computational chemistry has drawn much attention, due to the tardy improvement of central processing units (CPUs) and the more and more vibrant GPU software ecosystem, including electronic structure calculation,<sup>41-43</sup> classical/ab initio molecular dynamics,<sup>44-46</sup> and open system quantum dynamics.<sup>47,48</sup> In 2011, Kao *et al.* studied how GPU could accelerate tensor contraction in a tensor network and found the speedup of 20 times.<sup>49</sup> However, their research is not directly related to the DMRG algorithms. To the best of our knowledge, the only attempt to employ GPUs in DMRG was made by Nemes *et al.* in 2014.<sup>50</sup> They came up with a smart implementation exploiting both CPU and GPU which speeds up the Davidson diagonalization part in DMRG algorithm by 2 to 5 times. Despite their efforts, how GPUs can accelerate TD-DMRG algorithms remains unclear. Another issue about GPUs is the impact of float point precision on TD-DMRG calculations. As GPUs are originally designed for image rendering, most GPUs are focused on supporting single precision (SP) float point number operation rather than double precision (DP). The other advantage of SP over DP is that SP saves half memory with respect to DP, which could be prominent considering GPU memory is much more expensive than host memory. Pure SP or SP/DP hybrid precision has been proved useful in Hartree-Fock, coupled-cluster, density functional and molecular

dynamics calculations<sup>51–53</sup> while related research on TD-DMRG is still lacking.

To benchmark the accuracy and efficiency of the TD-DMRG time evolution schemes, a proper model should be chosen. In this work, we mainly focus on the vibronic coupling system. Therefore, we select the Fenna-Matthews-Olson (FMO) complex from green sulfur bacteria, which is an extremely popular system for both experimental and theoretical studies of energy transfer in photosynthesis.<sup>15,54,55</sup> The FMO model is described as a “guinea pig” of exciton dynamics<sup>16</sup> for comparing different computational methods since its exciton dynamics has been studied by many numerically exact methods, including quasi-adiabatic propagator path integral (QUAPI),<sup>56</sup> hierarchical equations of motion (HEOM),<sup>57,58</sup> ML-MCTDH<sup>59,60</sup> and TD-DMRG.<sup>16</sup>

In this paper, we select three time evolution schemes in TD-DMRG to simulate the exciton dynamics of 7-site FMO model, including P&C scheme with classical 4th order Runge-Kutta solver (P&C-RK4), TDVP with advanced matrix unfolding regularization algorithm (TDVP-MU) and PS scheme. We do not select TST scheme because TST is closely related to PS in a DMRG-inspired view, which we will discuss in detail below. With the three different schemes, we explore how the bond dimension  $M$  and time step size  $dt$  affect the outcomes of the dynamic simulations, and then we compare the accuracy of them. Finally, we set out to study the computational costs on different hardware architecture, including single/multi-core CPU and CPU-GPU heterogeneous computing. The influence of float point number precision on the accuracy and computational costs is also discussed.

## 2 Methodological Approaches

### 2.1 MPS and MPO Representation and TD-DMRG Algorithms

In the language of matrix product states (MPS),<sup>61</sup> a quantum state  $|\Psi\rangle$  under certain basis  $|\sigma_1\sigma_2\cdots\sigma_N\rangle$  can be represented as the product of a matrix chain, known as an MPS:

$$|\Psi\rangle = \sum_{\{a\},\{\sigma\}} A_{a_1}^{\sigma_1} A_{a_1 a_2}^{\sigma_2} \cdots A_{a_{N-1}}^{\sigma_N} |\sigma_1 \sigma_2 \cdots \sigma_N\rangle \quad (1)$$

where  $A_{a_{i-1} a_i}^{\sigma_i}$  are matrices in the chain connected by indices  $a_i$ ,  $\{\cdot\}$  represents the contraction of the respective connected indices, and  $N$  is the total number of matrices in the chain. The dimension of  $a_i$  is called bond dimension denoted as  $M$  or  $|a_i|$ , while the dimension of  $\sigma_i$  is called physical dimension denoted as  $d$ . Similarly, a quantum operator could also be expressed as a matrix product operator (MPO):<sup>61,62</sup>

$$\hat{O} = \sum_{\{a\},\{\sigma\},\{\sigma'\}} W_{a_1}^{\sigma_1, \sigma'_1} W_{a_1 a_2}^{\sigma_2, \sigma'_2} \cdots W_{a_{N-1}}^{\sigma_N, \sigma'_N} |\sigma_1 \sigma_2 \cdots \sigma_N\rangle \langle \sigma'_N \sigma'_{N-1} \cdots \sigma'_1| \quad (2)$$

When an MPO is applied to an MPS, a new MPS with larger bond dimension is produced:

$$\hat{O}|\Psi\rangle = \sum_{\{a, a'\}, \{\sigma\}} A_{\{a, a'\}_1}^{\sigma_1} A_{\{a, a'\}_1 \{a, a'\}_2}^{\sigma_2} \cdots A_{\{a, a'\}_{N-1}}^{\sigma_N} |\sigma_1 \sigma_2 \cdots \sigma_N\rangle \quad (3)$$

where

$$A_{\{a, a'\}_{i-1} \{a, a'\}_i}^{\sigma_i} = \sum_{\sigma'_i} W_{a_{i-1} a_i}^{\sigma_i, \sigma'_i} A_{a'_{i-1} a'_i}^{\sigma'_i} \quad (4)$$

Suppose the bond dimensions of the original MPS and the MPO are  $M_S$  and  $M_O$  respectively, then the new state has bond dimension  $M_O M_S$ .

The matrix product representation is usually not unique and a gauge condition can be applied to obtain a “mixed-canonical” MPS:

$$|\Psi\rangle = \sum_{\{a\},\{\sigma\}} A_{a_1}^{\sigma_1} A_{a_1 a_2}^{\sigma_2} \cdots A_{a_{n-2} a_{n-1}}^{\sigma_{n-1}} C_{a_{n-1} a_n}^{\sigma_n} B_{a_n a_{n+1}}^{\sigma_{n+1}} \cdots B_{a_{N-1}}^{\sigma_N} |\sigma_1 \sigma_2 \cdots \sigma_N\rangle \quad (5)$$

where  $A_{a_{i-1}a_i}^{\sigma_i}$  and  $B_{a_{i-1}a_i}^{\sigma_i}$  satisfy:

$$\sum_{\sigma_i, a_{i-1}} A_{a_{i-1}a'_i}^{\sigma_i*} A_{a_{i-1}a_i}^{\sigma_i} = \delta_{a'_i, a_i} \quad (6)$$

$$\sum_{\sigma_i, a_i} B_{a'_{i-1}a_i}^{\sigma_i*} B_{a_{i-1}a_i}^{\sigma_i} = \delta_{a'_{i-1}, a_{i-1}} \quad (7)$$

here  $A(B)^*$  represents the conjugate of  $A(B)$ . Then, we could define the renormalized basis as

$$|a_{n-1}\rangle_L = \sum_{\{a\}, \{\sigma\}} A_{a_1}^{\sigma_1} A_{a_1 a_2}^{\sigma_2} \cdots A_{a_{n-2} a_{n-1}}^{\sigma_{n-1}} |\sigma_1 \cdots \sigma_{n-1}\rangle \quad (8)$$

$$|a_n\rangle_R = \sum_{\{a\}, \{\sigma\}} B_{a_n a_{n+1}}^{\sigma_{n+1}} \cdots B_{a_{N-1}}^{\sigma_N} |\sigma_{n+1} \cdots \sigma_N\rangle \quad (9)$$

With Eq. 6 and 7, it is easy to check  $\langle a_{n-1} | a'_{n-1} \rangle_L = \delta_{a_{n-1}, a'_{n-1}}$  and  $\langle a_n | a'_n \rangle_R = \delta_{a_n, a'_n}$ . When there are only  $A(B)$  and  $C$  in the MPS, the state is called left(right)-canonical state. Canonical states can be prepared by performing sequential QR decomposition on any initial MPS, which is called canonicalisation.

A left(right)-canonical MPS  $|\Psi\rangle$  can be “compressed” as  $|\tilde{\Psi}\rangle$  by successive approximate Schmidt decomposition from the right(left)-most matrix to the left(right)-most matrix. After each local step of the compression,  $\| |\Psi\rangle - |\tilde{\Psi}\rangle \|$  is smaller than a reasonable value such as  $1 \times 10^{-3}$  but the bond dimension of the approximate MPS  $M_{|\tilde{\Psi}\rangle}$  is much smaller than  $M_{|\Psi\rangle}$ . Suppose we are sweeping from left to right, a local step of the compression has the following

form:

$$\begin{aligned}
|\Psi\rangle &= \sum_{\{a\},\{\sigma\}} A_{a_1}^{\sigma_1} \cdots A_{a_{n-2}a_{n-1}}^{\sigma_{n-1}} C_{a_{n-1}a_n}^{\sigma_n} B_{a_n a_{n+1}}^{\sigma_{n+1}} \cdots B_{a_{N-1}}^{\sigma_N} |\sigma_1 \cdots \sigma_N\rangle \\
&= \sum_{\{a\},\{\sigma\}} A_{a_1}^{\sigma_1} \cdots A_{a_{n-2}a_{n-1}}^{\sigma_{n-1}} \sum_s U_{a_{n-1}s}^{\sigma_n} S_{ss} V_{sa_n}^\dagger B_{a_n a_{n+1}}^{\sigma_{n+1}} \cdots B_{a_{N-1}}^{\sigma_N} |\sigma_1 \cdots \sigma_N\rangle \\
&\approx \sum_{\{a\},\{\sigma\}} A_{a_1}^{\sigma_1} \cdots A_{a_{n-2}a_{n-1}}^{\sigma_{n-1}} \sum_{a'_n} U_{a_{n-1}a'_n}^{\sigma_n} \left( S_{a'_n a'_n} V_{a'_n a_n}^\dagger B_{a_n a_{n+1}}^{\sigma_{n+1}} \right) \cdots B_{a_{N-1}}^{\sigma_N} |\sigma_1 \cdots \sigma_N\rangle \quad (10) \\
&= \sum_{\{a\},\{\sigma\}} A_{a_1}^{\sigma_1} \cdots A_{a_{n-2}a_{n-1}}^{\sigma_{n-1}} \sum_{a'_n} U_{a_{n-1}a'_n}^{\sigma_n} C_{a'_n a_{n+1}}^{\sigma_{n+1}} \cdots B_{a_{N-1}}^{\sigma_N} |\sigma_1 \cdots \sigma_N\rangle \\
&= \sum_{\{a,a'_n\},\{\sigma\}} A_{a_1}^{\sigma_1} \cdots A_{a_{n-2}a_{n-1}}^{\sigma_{n-1}} A_{a_{n-1}a'_n}^{\sigma_n} C_{a'_n a_{n+1}}^{\sigma_{n+1}} \cdots B_{a_{N-1}}^{\sigma_N} |\sigma_1 \cdots \sigma_N\rangle
\end{aligned}$$

where  $C_{a_{n-1}a_n}^{\sigma_n} = \sum_s U_{a_{n-1}s}^{\sigma_n} S_{ss} V_{sa_n}^\dagger$  is the singular value decomposition (SVD) and  $\{a, a'_n\}$  represents summing over  $a$  with  $a_n$  replaced by  $a'_n$ . After the compression, the dimension of  $a'_n$  ( $|a'_n|$ ) is much smaller than  $s$  ( $|s|$ ). Apart from truncation based on pre-determined  $M$ ,  $|a'_n|$  can be adaptively controlled according to a certain cutoff threshold  $\zeta$  such that only the renormalized basis whose  $S_{ss}$  is larger than  $\zeta$  will be retained. If  $|a'_n| = |s|$ , then no approximation is made and the procedure returns back to the above canonicalisation procedure where SVD could be replaced with QR decomposition for a better performance.

In the next subsections, we present the basic ideas and practical algorithms of three different TD-DMRG time evolution schemes adopted in our benchmark calculations afterwards: P&C-RK4,<sup>13,24</sup> TDVP-MU<sup>63,64</sup> and PS.<sup>32,65</sup> For more details, the readers are referred to the original papers of these methods.

### 2.1.1 P&C scheme

The P&C scheme is arguably the most direct time evolution scheme in MPS/MPO representation. If  $|\Psi(t)\rangle$  and the time derivative of  $|\Psi(t)\rangle$  are explicitly known (according to Schrödinger equation, the time derivative is  $-i\hat{H}\Psi$ ), any solver for the initial value problem (IVP) such as RK4 we use here, could be applied to obtain the MPS of the next time step

$|\Psi(t + dt)\rangle$ . For time independent Hamiltonian, the RK4 algorithm is nothing more than a 4th order Taylor expansion of the propagator  $e^{-iHdt}$  :

$$|\Psi(t + dt)\rangle = \sum_{n=0}^4 \frac{1}{n!} (-i\hat{H}dt)^n |\Psi(t)\rangle + O(dt^5) \quad (11)$$

The implementation based on MPS and MPO is quite straight-forward.  $\hat{H}|\Psi(t)\rangle$  is computed by applying  $\hat{H}$  to  $|\Psi(t)\rangle$  according to Eq. 3 and then the new MPS is compressed using algorithm based on the idea of Eq. 10 to reduce the bond dimension. It is worth noting that as the new MPS  $|\hat{H}\Psi(t)\rangle$  is not canonical, canonicalisation should be carried out before the actual compression. The compressed  $|\widetilde{\hat{H}\Psi(t)}\rangle$  should have similar bond dimension with the original MPS  $|\Psi(t)\rangle$ . Then starting from  $|\widetilde{\hat{H}\Psi(t)}\rangle$ , the higher order terms are calculated following the same logic. After that, these MPS are scaled by their coefficient and summed together. The bond dimension of the summed MPS is roughly 5 times of the bond dimension of the original MPS, so another canonicalisation-compression is performed to ensure that the bond dimension before and after the evolution remains precisely or roughly constant. Besides P&C-RK4 scheme, the other specific P&C schemes such as P&C-Krylov subspace<sup>24</sup> and P&C-chebyshev,<sup>25</sup> all take advantage of the compact MPS and MPO structure to represent the wavefunction and operator (Hamiltonian or propagator) respectively. Compared to the local evolution scheme as TST, P&C scheme could exactly represent the operation of high order Hamiltonian such as  $\hat{H}^n|\Psi\rangle$ . In the end, it is worth mentioning that though the P&C scheme is in principle a general evolution method for TD-DMRG, it prefers Hamiltonian whose MPO is easy to construct and has small bond dimension, such as Frenkel-Holstein model.<sup>13</sup>

### 2.1.2 TDVP-MU scheme

The TDVP-MU scheme originates from the standard TDVP-derived EOMs for the evolution of MCTDH wavefunction.<sup>33-35</sup> Due to the similar tensor network structure of DMRG and



MCTDH,<sup>38,66</sup> TDVP could also be used to evolve TD-DMRG wavefunction. Assuming that the time dependent MPS is fixed to be left-canonical, the rightmost site  $C_{a_{N-1}}^{\sigma_N}$  serves as a coefficient matrix with respect to the orthogonal renormalized basis  $|a_{N-1}\rangle_L$  constructed from site 1 to  $N-1$  and the other sites  $A_{a_{n-1}a_n}^{\sigma_n}$  serve as the local basis renormalizer, which is called single particle function (SPF) in MCTDH.<sup>35</sup> The EOMs are

$$i \frac{\partial C_{a_{N-1}}^{\sigma'_N}}{\partial t} = \sum_{\sigma_N, a_{N-1}} [H]_{a'_{N-1}, \sigma'_N, \sigma_N, a_{N-1}}^{(N)} C_{a_{N-1}}^{\sigma_N} \quad (12)$$

$$i \frac{\partial A_{a'_{n-1}a''_n}^{\sigma''_n}}{\partial t} = \sum_{a'_{n-1}, \sigma'_n} (1 - \hat{P}_{a'_{n-1}, \sigma'_n, \sigma''_n, a''_{n-1}}^{(n)}) \sum_{a'_n} \left( \rho_{a'_n, a''_n}^{(n)} \right)^{-1} \sum_{\sigma_n, a_{n-1}, a_n} [H]_{a'_{n-1}, a_{n-1}, \sigma'_n, \sigma_n, a'_n, a_n}^{(n)} A_{a_{n-1}a_n}^{\sigma_n} \quad (13)$$

where:

$$[H]_{a'_{n-1}, a_{n-1}, \sigma'_n, \sigma_n, a'_n, a_n}^{(n)} = \sum_{\{a\}, \{b\}, \{a'\}} [L]_{\{a', b, a\}_{n-1}}^{(n-1)} H_{b_{n-1}b_n}^{\sigma_n, \sigma'_n} [R]_{\{a', b, a\}_n}^{(n)} \quad (14)$$

$$[L]_{\{a', b, a\}_{n-1}}^{(n-1)} = \sum_{\{a\}, \{b\}, \{a'\}} [h]_{\{a', b, a\}_1}^{(1)} \cdots [h]_{\{a', b, a\}_{n-2}, \{a', b, a\}_{n-1}}^{(n-1)} \quad (15)$$

$$[R]_{\{a', b, a\}_n}^{(n)} = \sum_{\{a\}, \{b\}, \{a'\}} [h]_{\{a', b, a\}_n, \{a', b, a\}_{n+1}}^{(n+1)} \cdots [h]_{\{a', b, a\}_{N-1}}^N \quad (16)$$

$$[h]_{\{a', b, a\}_{n-1}, \{a', b, a\}_n}^{(n-1)} = \sum_{\sigma_n, \sigma'_n} A_{a'_{n-1}a'_n}^{\sigma'_n *} H_{b_{n-1}b_n}^{\sigma_n, \sigma'_n} A_{a_{n-1}a_n}^{\sigma_n} \quad (17)$$

$$\hat{P}_{a'_{n-1}, \sigma'_n, \sigma_n, a_{n-1}}^{(n)} = \sum_{a_n} A_{a'_{n-1}a_n}^{\sigma'_n *} A_{a_{n-1}a_n}^{\sigma_n} \quad (18)$$

$$\rho_{a'_n, a_n}^{(n)} = \sum_{\{a\}, \{a'\}, \{\sigma\}} (A_{a'_n a'_{n+1}}^{\sigma_{n+1}} A_{a'_{n+1} a'_{n+2}}^{\sigma_{n+2}} \cdots C_{a'_{N-1}}^{\sigma_N})^* (A_{a_n a_{n+1}}^{\sigma_{n+1}} A_{a_{n+1} a_{n+2}}^{\sigma_{n+2}} \cdots C_{a_{N-1}}^{\sigma_N}) \quad (19)$$

With the EOMs in hand, the matrices are propagated one by one based on the constant mean field (CMF) scheme<sup>35</sup> using the common IVP solver which in our case is adaptive

Runge–Kutta–Fehlberg (RKF) solver. An important technique to reduce the computational cost when calculating the time derivatives is to contract small matrices one by one instead of explicitly constructing the large tensor  $[H]_{a'_{n-1}, a_{n-1}, \sigma'_n, \sigma_n, a'_n, a_n}^{(n)}$ , which effectively reduces the number of float point operation required to complete the computation. This evolution scheme has been firstly explored in 2011,<sup>31</sup> but did not gain widespread acceptance in practical application. One main important reason is that the inverse of the density matrix  $\rho$  in Eq. 13 is numerically unstable, especially when the state is weakly correlated and  $M$  is much larger than required such as a Hartree product state. To some extent, this instability problem makes this evolution scheme paradoxical in that large  $M$  should in principle push the result to a numerically exact limit but in fact deteriorates it.

To partially remove the singularity of  $\rho$ , we use the matrix unfolding (MU) method proposed by Meyer and Wang recently in (ML-)MCTDH,<sup>63,64</sup> which is superior to the original regularization algorithm.<sup>35</sup> The key point of MU is that for a mixed-canonical MPS in Eq. 5,  $C_{a_{n-1}a_n}^{\sigma_n}$  is firstly decomposed into  $\sum_s U_{a_{n-1}s}^{\sigma_n} S_{ss} V_{sa_n}^\dagger$  by SVD and  $U_{a_{n-1}s}^{\sigma_n}$  plays the role of basis renormalizer as  $A$ . Because of the right-canonical structure on the right side of  $C$  and  $V^\dagger V = I$ , the density matrix  $\rho^{(n)}$  is reduced to  $\rho_{s's'}^{(n)} = S_{ss}^2 \delta_{s,s'}$ . Following Eq. 13, the EOM for  $U_{a_{n-1}s}^{\sigma_n}$  in TDVP-MU scheme is

$$i \frac{\partial U_{a_{n-1}s'}^{\sigma_n''}}{\partial t} = \sum_{a'_{n-1}, \sigma'_n} (1 - \hat{P}_{a'_{n-1}, \sigma'_n, \sigma_n'', a''_{n-1}}^{(n)}) S_{s's'}^{-1} (\underline{S_{s's'}^{-1} S_{s's'}}) \sum_{\sigma_n, a_{n-1}, s} \left\{ \sum_{a_n, a'_n} V_{s'a'_n}^{\dagger*} [H]_{a'_{n-1}, a_{n-1}, \sigma'_n, \sigma_n, a'_n, a_n}^{(n)} S_{ss} V_{sa_n}^\dagger \right\} U_{a_{n-1}s}^{\sigma_n} \quad (20)$$

Apparently, the underlined part satisfies  $S_{s's'}^{-1} S_{s's'} = 1$ . Thus, only the quasi-singular matrix  $S_{ss}$  needs to be regularized by adding small values around  $\varepsilon$  giving  $\tilde{S}_{ss}$ :

$$\tilde{S}_{ss} = S_{ss} + \varepsilon^{1/2} e^{-S_{ss}/\varepsilon^{1/2}} \quad (21)$$

The power 1/2 here is for consistency with the original regularization algorithm.<sup>35</sup> Note that

$S_{ss}$  and  $\varepsilon$  are both positive, so  $e^{-S_{ss}/\varepsilon^{1/2}} \in (0, 1)$ . In this work we choose  $\varepsilon = 1 \times 10^{-10}$  unless otherwise stated. Compared to the original EOM in Eq. 13, the EOM in Eq. 20 is more stable and allows much larger time step than the original regularization method, because the condition number of  $S$  is approximately the square root of that of  $\rho$ .

In summary, the overall procedure is illustrated as follows, assuming starting from Eq. 5 and sweeping from left to right. Firstly,  $[L]_{\{a',b,a\}_{n-1}}^{(n-1)}$  and  $[R]_{\{a',b,a\}_n}^{(n)}$  are computed by matrix multiplication and the previously retained tensors such as  $[L]_{\{a',b,a\}_{n-2}}^{(n-2)}$  and  $[R]_{\{a',b,a\}_{n+1}}^{(n+1)}$  are used when possible. Subsequently,  $U_{a_{n-1}s}^{\sigma_n}$  is propagated according to Eq. 20 by RKF algorithm. Finally  $\tilde{S}_{ss}V_{sa_n}^\dagger$  is absorbed into  $B_{a_n a_{n+1}}^{\sigma_{n+1}}$  resulting in  $C_{sa_{n+1}}^{\sigma_{n+1}}$ . As  $U_{a_{n-1}s}^{\sigma_n}$  satisfies the left-canonical condition Eq. 6, we can rewrite  $U_{a_{n-1}s}^{\sigma_n}$  as  $A_{a_{n-1}s}^{\sigma_n}$  and get the following MPS:

$$\sum_{\{a,s\},\{\sigma\}} A_{a_1}^{\sigma_1} \cdots A_{a_{n-2}a_{n-1}}^{\sigma_{n-1}} A_{a_{n-1}s}^{\sigma_n} C_{sa_{n+1}}^{\sigma_{n+1}} B_{a_{n+1}a_{n+2}}^{\sigma_{n+2}} \cdots B_{a_{N-1}}^{\sigma_N} |\sigma_1 \cdots \sigma_N\rangle \quad (22)$$

where  $|s| = |a_n|$ . Thus the MPS is restored to the form of Eq. 5 with the  $n$ th site propagated, and we can move on to evolve  $C_{sa_{n+1}}^{\sigma_{n+1}}$  with exactly the same procedure.

### 2.1.3 PS scheme

The derivation and implementation of the PS scheme are more complicated.<sup>32</sup> In short, the TDVP is equivalent to that the time derivative of an MPS  $|\Psi\rangle$  is projected onto the tangent space of the MPS manifold  $\mathcal{M}_{\text{MPS}}$ :

$$\frac{\partial |\Psi\rangle}{\partial t} = -i\hat{P}_{T_{|\Psi\rangle}\mathcal{M}_{\text{MPS}}}\hat{H}|\Psi\rangle \quad (23)$$

The projector  $\hat{P}_{T|\Psi\rangle, \mathcal{M}_{\text{MPS}}}$  has the form:

$$\begin{aligned} \hat{P}_{T|\Psi\rangle, \mathcal{M}_{\text{MPS}}} &= \sum_{n=1}^N \left\{ \sum_{a_{n-1}} |a_{n-1}\rangle \langle a_{n-1}|_L \otimes \hat{I}_n \otimes \sum_{a'_n} |a'_n\rangle \langle a'_n|_R \right\} \\ &\quad - \sum_{n=1}^{N-1} \left\{ \sum_{a_n} |a_n\rangle \langle a_n|_L \otimes \sum_{a'_n} |a'_n\rangle \langle a'_n|_R \right\} \end{aligned} \quad (24)$$

where  $|a_{n-1}\rangle_L$  and  $|a'_n\rangle_R$  are define in Eq. 8. Taking advantage of the locality of the projector, the formal propagator  $e^{-i\hat{P}_{T|\Psi\rangle, \mathcal{M}_{\text{MPS}}}\hat{H}dt}$  is split by Trotter decomposition into two sets of local propagators. Corresponding to the projector in Eq. 24, one set is in the local renormalized space  $|a_{n-1}\rangle_L |\sigma_n\rangle |a'_n\rangle_R$  with forward  $t$  and the other set is in the local renormalized space  $|a_n\rangle_L |a'_n\rangle_R$  with backward  $-t$ . Here, other than deriving the projector in Eq. 24 rigorously, we would like to give an intuitive understanding of the PS method in a DMRG-inspired view. We will first recap the idea of the TST method proposed by White *et al.*,<sup>27</sup> because to some extent TST and PS have a similar DMRG philosophy.<sup>2</sup>

In TST with one-site algorithm, at the active center  $n$  in a mixed-canonical MPS in Eq. 5, the local coefficient matrix  $C_{a_{n-1}a_n}^{\sigma_n}$  is evolved in the renormalized space  $|a_{n-1}\rangle_L |\sigma_n\rangle |a'_n\rangle_R$ . After that, the averaged reduced density matrix is constructed by including state  $|\Psi(t)\rangle$ ,  $|\Psi(t+dt)\rangle$  and some other intermediate states, and then a set of adapted basis is obtained to describe the time window  $t \rightarrow t+dt$ . However, only  $|\Psi(t)\rangle$  is adapted (or projected) to these renormalized basis to obtain an approximate  $|\tilde{\Psi}(t)\rangle$  and at the same time move the active center to the next site. This single step process could be expressed as  $\hat{P}_{1\rightarrow 2} e^{i\hat{H}_1 dt} e^{-i\hat{H}_1 dt} |\Psi(t)\rangle$ , where the subscript 1 represents the renormalized space  $|a_{n-1}\rangle_L |\sigma_n\rangle |a'_n\rangle_R$  at site  $n$  and the subscript 2 represents the renormalized space  $|a_n\rangle_L |a'_n\rangle_R$  between site  $n$  and site  $n+1$  after site  $n$  adapted. After several sweeps, assuming all the local matrices are adapted well in this time window, the final active center (usually the site in the center of the MPS) is propagated forward from  $t$  to  $t+dt$ . There are two key points in the TST method, one is that only  $|\Psi(t)\rangle$  is projected onto the adapted basis to avoid double counting when evolving the next

site. The other is that the adapted basis is constructed from the averaged density matrix.

In the PS method, at the active center  $n$ ,  $C_{a_{n-1}a_n}^{\sigma_n}$  is firstly evolved to  $|\Psi(t+dt)\rangle$  as TST. After that, unlike TST, the reduced density matrix is constructed from  $|\Psi(t+dt)\rangle$  alone and  $|\Psi(t+dt)\rangle$  is adapted to the new renormalized basis without truncation error. Then,  $|\Psi(t+dt)\rangle$  is evolved backward in the renormalized space  $|a_n\rangle_L |a'_n\rangle_R$  to obtain  $|\tilde{\Psi}(t)\rangle$ . This single step process could be expressed as  $e^{i\hat{H}_2 dt} \hat{P}_{1\rightarrow 2} e^{-i\hat{H}_1 dt} |\Psi(t)\rangle$ , where the space 2 is distinct from that of TST as a result of the different way to construct the reduced density matrix. Besides the difference in obtaining space 2, the other difference of TST and PS lies in the order to apply the projector  $\hat{P}_{1\rightarrow 2}$  and the backward propagator  $e^{i\hat{H} dt}$ , since these two operations do not commute. Except these two points above, TST and PS obviously share a rather similar evolution strategy from a DMRG-inspired view that three local sub-steps are subtly arranged including evolving forward, evolving backward and adapting the basis. As a result, both TST and PS perform well in the existing numerical examples.<sup>10,11,16,27</sup> However, only PS has a rigorous mathematical foundation and that is why we choose PS for comparison.

In summary, the overall procedure of PS scheme is illustrated as follows, assuming starting from Eq. 5 and sweeping from left to right. Firstly,  $C_{a_{n-1}a_n}^{\sigma_n}$  is evolved forward similar to Eq. 12:

$$i \frac{\partial C_{a'_{n-1}a'_n}^{\sigma'_n}}{\partial t} = \sum_{\sigma_n, a_{n-1}, a_n} [H]_{a'_{n-1}, a_{n-1}, \sigma'_n, \sigma_n, a'_n, a_n}^{(n)} C_{a_{n-1}a_n}^{\sigma_n} \quad (25)$$

Then, the evolved matrix  $C_{a_{n-1}a_n}^{\sigma_n}$  is decomposed by QR into  $\sum_s A_{a_{n-1}s}^{\sigma_n} D_{sa_n}$ . Among them,  $A_{a_{n-1}s}^{\sigma_n}$  serves as the adapted local matrix at site  $n$  which is left-canonical, while the coefficient matrix  $D_{sa_n}$  is further evolved backward in time to compensate the effect of the previous forward evolution, based on EOMs even simpler than Eq. 12:

$$i \frac{\partial D_{s'a'_n}}{\partial t} = \sum_{s, b, a_n} [L]_{\{s', b, s\}_n}^{(n)} [R]_{\{a', b, a\}_n}^{(n)} D_{sa_n} \quad (26)$$

After that,  $D_{sa_n}$  is merged into the next site to form  $C_{a_n a_{n+1}}^{\sigma_{n+1}}$  and the algorithm starts over

again from site  $n+1$ . During the whole sweep, the local evolution process is the same at every site except the rightmost one, where there is no  $D$  existed. To further improve the accuracy, the sweep could be performed from left to right within time window  $t \rightarrow t + 1/2dt$ , and then from right to left alternately within time window  $t + 1/2dt \rightarrow t + dt$  to make the single step evolution a second order method with respect to  $dt$ .<sup>32</sup> In principle, solving Eq. 25 and Eq. 26 on the single matrix in the PS scheme can be accomplished by any general IVP solver such as RKF method we used in TDVP-MU scheme. However, since all the EOMs are linear in the PS scheme, the Krylov subspace method is preferred as it is unitary and is considered to be better than the explicit time-stepping integrators.<sup>67</sup> In our calculation, the dimension of the Krylov subspace is adaptive and the Lanczos iteration continues until  $|\Psi(t + dt)\rangle$  converges (for each matrix element  $e_i$  of  $|\Psi(t + dt)\rangle$ ,  $\Delta e_i < 1 \times 10^{-8} + 1 \times 10^{-5} \times |e_i|$ ). On the contrary, the Krylov subspace method could not be applied in the TDVP-MU scheme except evolving the rightmost(leftmost) site when sweeping from left(right) to right(left), because Eq. 13 is nonlinear with  $A_{a_{n-1}n}^{\sigma_n}$ .

Compared to the TDVP-MU scheme, PS is free of the instability problem of matrix inversion. But the common one-site algorithm still requires to define a fixed  $M$  a priori. In addition, additional renormalized basis should be constructed by hand to fill the MPS space if the initial state is weakly correlated, which will influence the evolution especially during the initial short period. Fortunately, it is easy to formulate PS into two-site algorithm in TD-DMRG (not easy in the common ML-MCTDH if not impossible) so that the bond dimension could grow up automatically.<sup>32</sup> However, the two-site algorithm is much expensive than the one-site algorithm both in the matrix contraction and QR decomposition. Therefore, in our calculations we will use P&C-RK4 scheme to evolve for a while in the beginning in order to obtain a proper initial state for TDVP-MU and PS to start .

## 2.2 Multi-core CPU and CPU-GPU Heterogeneous Computing

The parallelism of DMRG algorithms over multiple cores has attracted much interest<sup>68,69</sup> and nearly linear scaling speedups are reported.<sup>70</sup> Although some of them can be merged into TD-DMRG algorithms, in this paper we are only concerned with the simplest form of parallelism, which is breaking up dense matrix computations into subblocks performed automatically by the standard linear algebra libraries. In our calculations, we set environment variables to control the maximum number of CPU cores these libraries are allowed to use. When GPU is incorporated in the calculation, we store the matrices on GPU memory instead of in host memory, and in most cases call cuBLAS to manipulate them except when doing matrix decomposition such as QR or SVD which is not the ideal workload for GPUs. In such cases we first transfer the matrix from GPU memory to host memory and then use a single CPU core to complete the decomposition, and in the end copy the matrix back. The overhead caused by data transfer is not negligible which we believe could be avoided by a smarter implementation because GPUs are able to run computation and data transfer at the same time. In the following calculation, only one GPU is used for each time evolution calculation.

## 2.3 Computational Details of the FMO Model

The widely used Frenkel-Holstein Hamiltonian<sup>71,72</sup> to describe the 7-site FMO model<sup>73</sup> is that:

$$\begin{aligned} \hat{H} = & \sum_{mn} (\delta_{mn} E_m + J_{mn}) a_m^\dagger a_n + \sum_{m\lambda} \omega_{m\lambda} \left( b_{m\lambda}^\dagger b_{m\lambda} + \frac{1}{2} \right) \\ & + \sum_{m\lambda} g_{m\lambda} \omega_{m\lambda} \left( b_{m\lambda}^\dagger + b_{m\lambda} \right) a_m^\dagger a_m \end{aligned} \quad (27)$$

where  $a_m^\dagger$  ( $a_m$ ) is the exciton creation (annihilation) operator on the  $m$ th site whose local excitation energy is  $E_m$ ,  $J_{mn}$  is the Coulomb interaction between the  $m$ th and  $n$ th site,  $b_{m\lambda}^\dagger$  ( $b_{m\lambda}$ ) is the phonon creation (annihilation) operator of vibration mode  $\lambda$  of  $m$ th site with vibration frequency  $\omega_{m\lambda}$  and dimensionless electron-phonon coupling strength  $g_{m\lambda}$ . A diagram of the model is shown in Figure 1.

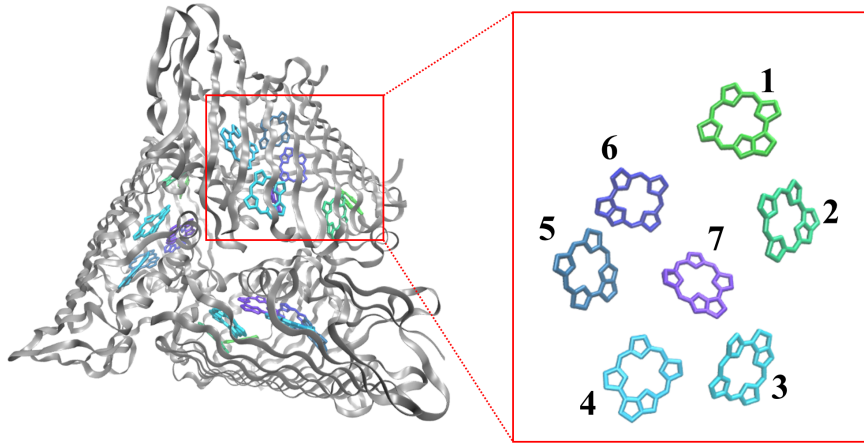


Figure 1: A diagram of the 7-site FMO model in our calculations.

We obtain  $E_m$  and  $J_{mn}$  from previous literature<sup>60,74</sup> and each site has a same environment with  $\omega_{m\lambda}$  and  $g_{m\lambda}$  calculated by discretization of the bath spectral density from experiments.<sup>60,75</sup> For each site, 35 vibration modes are discretized, giving 252 degrees of freedom (DOFs) in total (245 vibrational DOFs + 7 electronic DOFs). The dimension of basis space for each mode varies with frequency and most modes have 8 or 4 phonon occupation levels. To minimize the entanglement, the sites in the MPS chain are arranged in the order of [7, 5, 3, 1, 2, 4, 6] so that initially the exciton is placed at the center of the chain (site 1) and then gradually transfers to sites next to the boundary. All the local vibrational DOFs are arranged next to the local electronic site as our previous work.<sup>13</sup>

We first set up each vibrational DOF in the ground state of the local potential energy surface respectively and investigate the exciton dynamics at zero temperature. Figure 2 shows the population dynamics of the 7-site FMO model obtained by P&C-RK4 scheme with  $M = 64$  and  $dt = 160$  which is in quantitative agreement with previous reports.<sup>16,60</sup> For simplicity, through out this paper we use atomic unit (a.u.) as unit of time unless otherwise stated and omit the unit of  $t$  and  $dt$ .

As the initial state of the evolution is essentially a Hartree product ( $M = 1$ ), TDVP-based



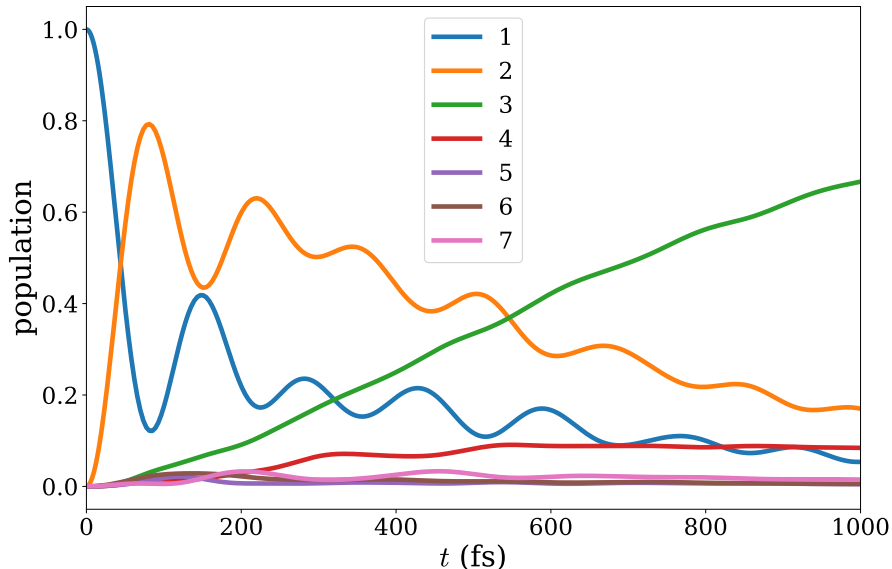


Figure 2: Population dynamics of the 7-site FMO model obtained with P&C-RK4 scheme.

methods (TDVP-MU and PS) should somehow find a proper set of renormalized orthogonal basis to occupy the empty matrices in the MPS before the evolution starts. To solve this, we use P&C-RK4 to propagate the state to  $t = 800$  with  $M = 256$  in the first 10 steps and then start the calculation of TDVP-based methods from this state. The required bond dimension is obtained by performing compression before the actual evolution begins.

We’ve also simulated the dynamics at finite temperature based on “purification” method.<sup>76,77</sup> In this formulation, the time evolution of density matrix is almost the same with time evolution of the pure state except that the physical dimension  $d$  for each matrix is squared. As the general trend at finite temperature is similar with that in zero temperature and the swelled computational cost prohibits systematic benchmark, these results are only shown in supporting information (Figure S2, S3, S4).

### 3 Results and Discussions

In this section we perform benchmarks on the accuracy and efficiency of the three time evolution schemes described in Section 2 with FMO model. How float point precision affect the results is analyzed in Section 3.2.2.

#### 3.1 Accuracy

An impartial metric for the accuracy of MPS  $|\Psi\rangle$  at time  $t$  is the distance between  $|\Psi(t)\rangle$  and another standard MPS  $|\Psi(t)\rangle_{\text{std}}$  denoted as  $\epsilon(t)$  representing error at  $t$ :

$$\epsilon(t) = || |\Psi(t)\rangle - |\Psi(t)\rangle_{\text{std}} || \quad (28)$$

Choosing an appropriate  $|\Psi(t)\rangle_{\text{std}}$  is of crucial importance in this approach since apparently an absolutely exact result could not be obtained. Here we rely on TD-DMRG methods to calculate  $|\Psi(t)\rangle_{\text{std}}$  and consider it as reasonably accurate if dynamics of physical observables have converged on both  $M$  and  $dt$ . Such convergence on the electronic occupation of the 7th pigment  $P^{(7)}$  for the PS method is illustrated in Figure 3. We are in favour of this observable because it has small absolute value so that the relative error is more visible. Figure 3a indicates that upon increasing  $M$ ,  $P^{(7)}$  becomes more and more accurate and converges at  $M = 128$  or  $M = 256$ , while in Figure 3b  $P^{(7)}$  is almost irrelevant with  $dt$ . Thus in the following we use MPS obtained with  $M = 256$  and  $dt = 160$  as the reference states. The reason why we don't use P&C-RK4 and TDVP-MU as reference is that they can't reach such perfect convergence within practical computational resource, which will be demonstrated later.

After  $|\Psi(t)\rangle_{\text{std}}$  is obtained, we can benchmark the accuracy of P&C-RK4, TDVP-MU and PS in a variety of  $M$  and  $dt$  combinations and a full collection of our data can be found in Figure S1 of the supporting information. To begin with, we focus on the P&C-RK4 scheme and  $\epsilon(t)$  as a function of  $t$  is plotted in the upper panel of Figure 4. We find that if  $dt$  is

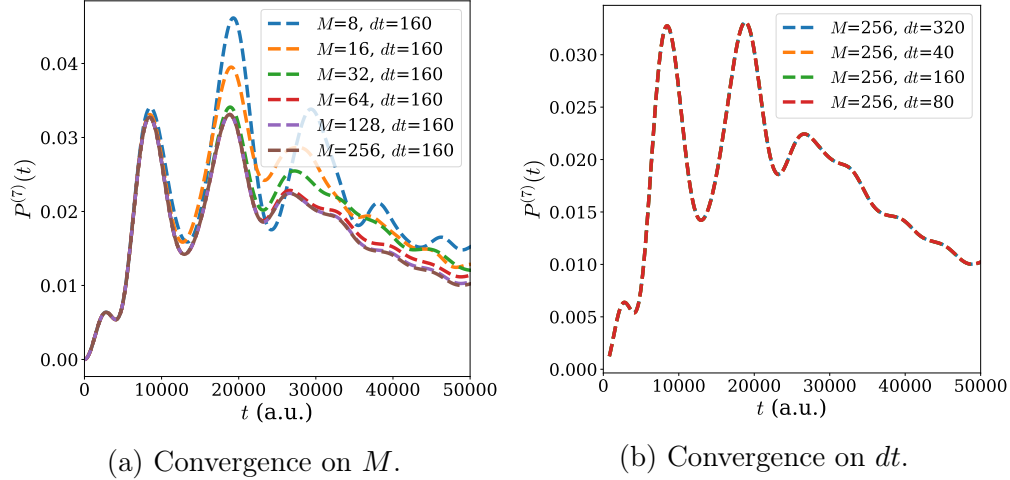


Figure 3: Numerical convergence on  $P^{(7)}$  of the PS method.

too large the evolution would diverge at some point, resulting in a totally wrong state that is orthogonal to the standard state conjectured by the distance of approximately  $\sqrt{2}$ . For time evolution that does not diverge,  $\epsilon(t)$  grows smoothly to values as large as about 1. By instinct we expect the error at this stage would be large, however the expectation values of physical observables such as exciton populations are still quite precise as shown in the lower panel of Figure 4. For clarity the diverged yellow curves are omitted after  $t = 18000$ . Although the  $\epsilon(t)$  and  $|P^{(1)}(t)/P_{\text{std}}^{(1)}(t) - 1|$  reflect the same tendency, the upper panel in Figure. 4 is noticeably more comprehensible than the lower panel and thus  $\epsilon(t)$  serves as a better metric for evaluating error.

Although Figure 4 is quite informative, it's difficult to read out the dependency of  $\epsilon(t)$  on  $M$  and  $dt$  at a glance, so we rearrange the data and present only  $\epsilon(\mathbf{t})$  where  $\mathbf{t} = 46880$ , which is shown in Figure 5. The accuracy monotonically improves with  $M$  as expected. However, the error first reduces and then grows with increasing  $dt$ . The decline is due to the reduced number of compression operations during the time evolution and the growth is probably due to that the time step is out of the stable region of RK4 solver<sup>13</sup> leading to the divergence shown in Figure 4. In every step of P&C-RK4 evolution, MPS compression has to be performed several times and each compression results in an insignificant local error. When the step size  $dt$  is very small, the error caused by the IVP solver RK4 is well controlled,

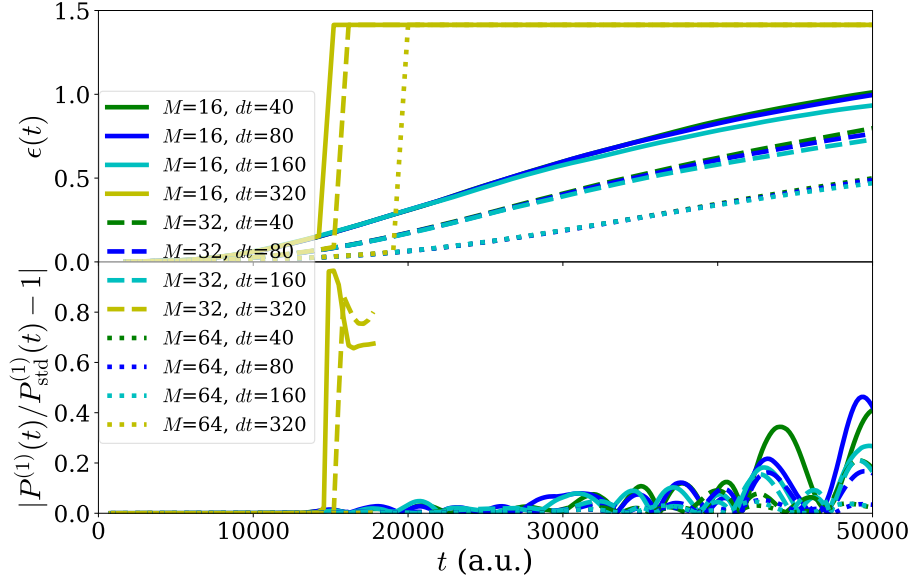


Figure 4: Accumulated error during time evolution of P&C-RK4 scheme. Upper panel: error measured by Eq. 28. Lower panel: error measured by relative error on the electronic occupation of the 1st pigment.

but the error caused by compression will accumulate more quickly and finally hampers the total accuracy. Based on these phenomena, an optimal strategy for choosing P&C-RK4 time evolution step size is to choose largest step size possible as long as the calculation does not diverge. It should be mentioned that in theory relatively large  $dt$  causes the RK4 solver to produce more error than DMRG compression. Thus there should be a region where  $\epsilon(t)$  is positively correlated with  $dt$ . In our case such region can be found when  $t$  is less than 20000 whose example is presented in Figure S5.

A major superiority of the P&C scheme is that in this scheme a truncation threshold  $\zeta$  can be used to allow dynamic growth of bond dimension during the time evolution. In Figure 6 we compare this approach with fixed bond dimension at  $dt = 160$ . The  $x$ -axis of the figure only extends to  $t = 25000$  because the bond dimension determined by truncation threshold has grown too large for practical computation at longer time scale. At  $t = 25000$ , the maximum  $M$  of the 3 solid curves are 23, 77 and 221 corresponding to  $\zeta = 0.002, 0.0005, 0.0001$  respectively. However the accuracy of the dynamic bond dimension approach is even lower,

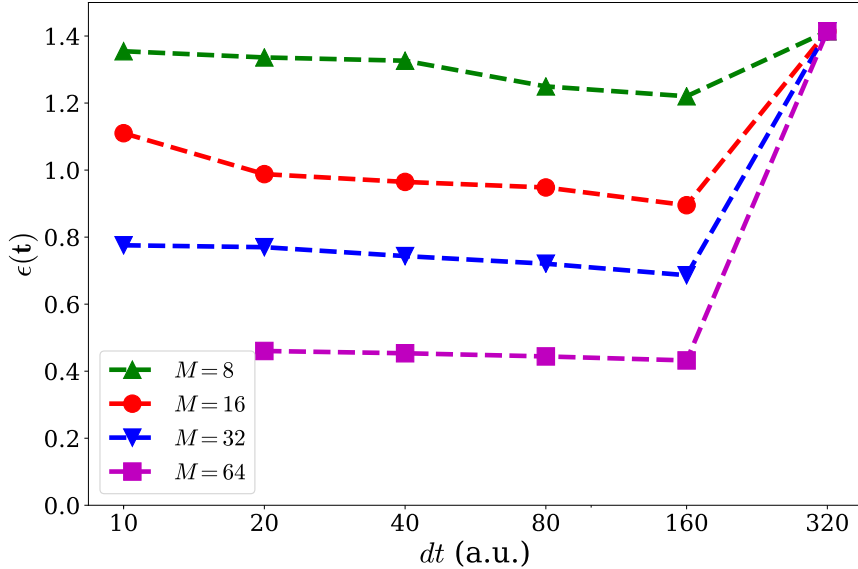


Figure 5: Relation between  $\epsilon(t)$  and  $dt$  with different  $M$  for the P&C-RK4 scheme. The  $x$  axis is in log scale.

such as  $\zeta = 0.0005$  (orange solid line, largest  $M$  equals 77) against  $M = 64$  (brown dashed line). It is probably owing to the relatively large error introduced when  $t$  and  $M$  are small and the large bond dimension at later time is wasted to describe these unphysical states established at the early stages.

For the TDVP-MU scheme, a diagram similar to Figure 5 is shown in Figure 7. With the same  $M$ ,  $\epsilon(t)$  in TDVP-MU scheme is in general smaller than  $\epsilon(t)$  in P&C-RK4 scheme. TDVP-MU also seems to tolerate larger  $dt$ . As P&C-RK4, the main contributor to the total error is the limited variational space under the control of  $M$ . However for a fixed  $M$ , in contrary with the P&C-RK4 scheme, the propagation of TDVP-MU scheme does not require any compression and therefore the main source of error is due to the CMF and the RKF solver with finite time step. That's why a larger time step size will lead to a less accurate result. Another contributor to the total error which is the inversion instability and regularization will be examined later when we discuss Figure 9, but it has little effect on the general tendency shown in Figure 7. Therefore for TDVP-MU calculations small  $dt$  should

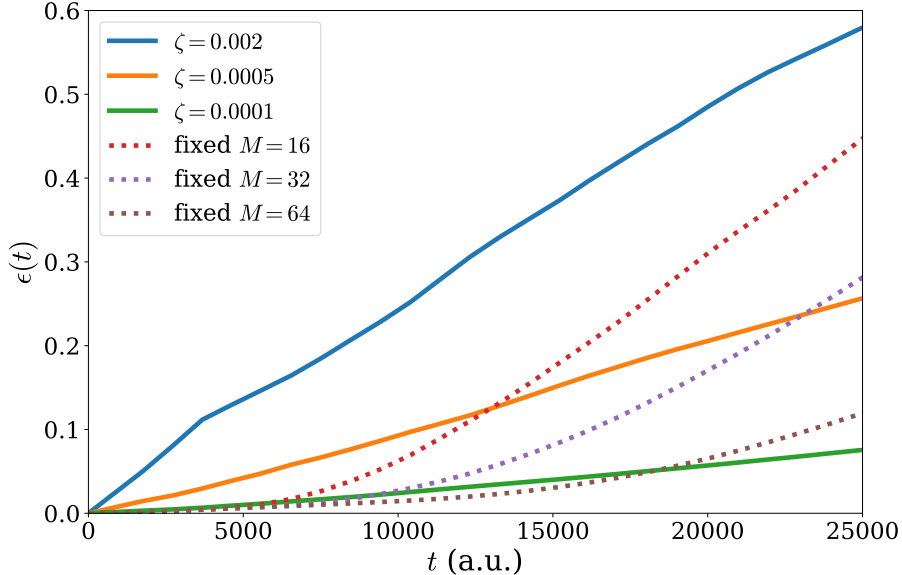


Figure 6: Comparison between fixed  $M$  and dynamic bond dimension controlled by truncation threshold  $\zeta$ .

be selected and it is more meaningful to be combined with a large  $M$ .

Then we examine the PS scheme in the same manner. In theory, as a scheme based on TDVP, larger time step will result in worse results. To our surprise, the PS scheme is extremely insensitive to  $dt$  and the result remains rather accurate even when  $dt = 2880$ . In other words, the Trotter error is very small and negligible when  $dt < 2880$ . We double-checked the accuracy of the results with such large  $dt$  and the population dynamics with  $dt = 5760$  and  $M = 160$  can be found in Figure S7. This outstanding performance comes with a moderate price. When  $dt = 160$ , 6 vectors in the Krylov space are well enough for converged evolution, whereas more than 50 vectors are required when  $dt = 5760$ . Simple math implies increasing  $dt$  when possible is still beneficial to computational cost. Apart from the time step, the PS scheme also reaches the highest accuracy among the 3 schemes for a given  $M$ , probably because the Krylov subspace algorithm is unitary which is not the case for RK solvers and the inexactitude caused by the inversion instability and regularization is perfectly eliminated. The PS scheme proves to be a fairly accurate and robust method and

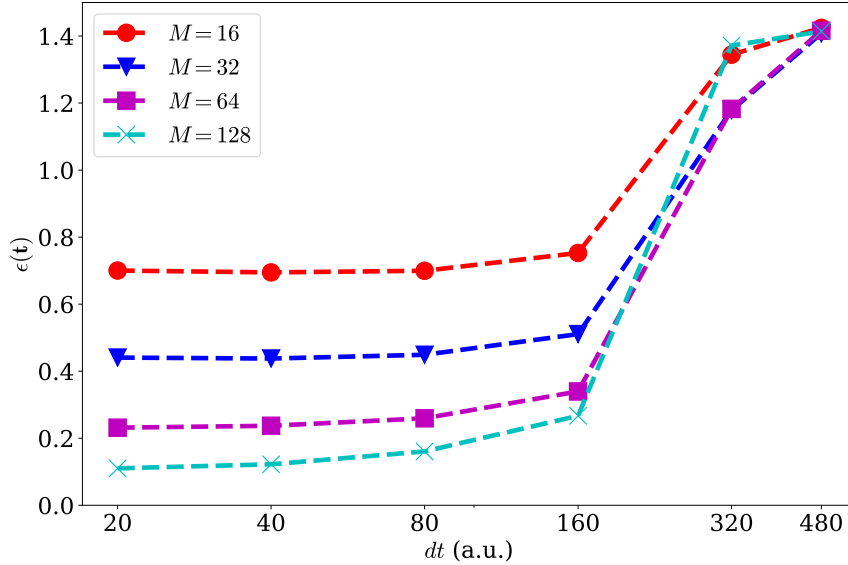


Figure 7: Relation between  $\epsilon(t)$  and  $dt$  with different  $M$  for TDVP-MU scheme. The  $x$  axis is in log scale.

$dt$  can be chosen from a very broad scope without precision deterioration.

Finally, we make a direct comparison of the 3 schemes for more insights.  $\epsilon(t)$  of the P&C-RK4 scheme and the TDVP-MU scheme with  $M = 64$  are shown in Figure 9a. The figure reproduces some observations we made earlier in this section, for example, the P&C-RK4 scheme and the TDVP-MU scheme are more accurate with larger  $dt$  and smaller  $dt$  respectively. One of the new insights from Figure 9a is that  $\epsilon(t)$  grows in distinct manners between the P&C-RK4 scheme and the TDVP-MU scheme. In the P&C-RK4 scheme, the accumulation of error is slow when  $t$  is less than about 15000 but the process is accelerated with longer evolution time. The overall behavior before 30000 a.u. seems like a quadratic curve. But for the TDVP-MU scheme  $\epsilon(t)$  is roughly linear with  $t$ . Another interesting fact is that at short  $t$  ( $< 10000$ ),  $\epsilon(t)$  of the TDVP-MU scheme increases more quickly, which is arguably due to the error introduced by the unstable inversion and artificial regularization. At longer  $t$  all states in the variational space have been numerically populated and the regularization error becomes insignificant. As a matter of fact, when the TDVP-MU scheme

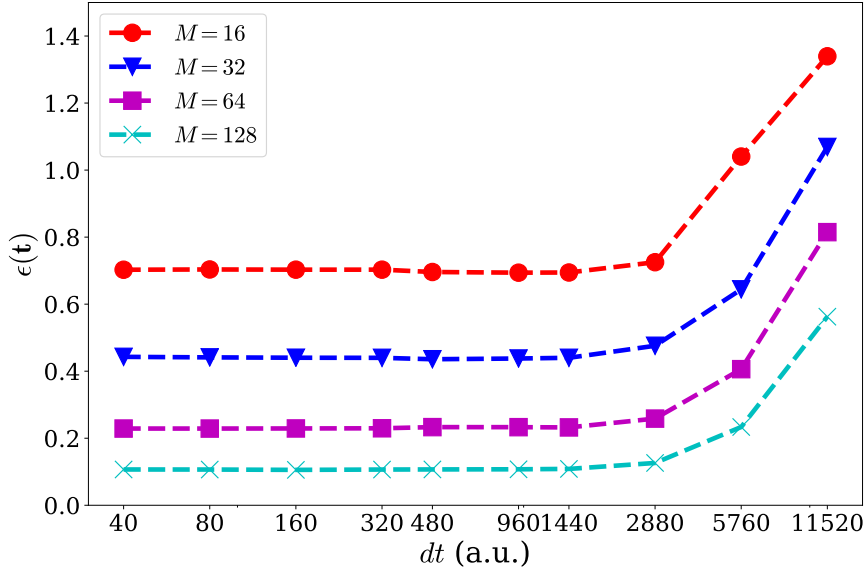


Figure 8: Relation between  $\epsilon(t)$  and  $dt$  with different  $M$  for PS scheme. The  $x$  axis is in log scale.

is compared with the PS scheme in Figure 9b with  $M = 64$ , the curves of the two schemes almost run in parallel at long time regardless of  $dt$  chosen because of that the two schemes essentially both rely on TDVP. The difference lies in the error accumulated in short time, which is probably due to the inversion instability and regularization of TDVP-MU.

Our conjecture is further supported by Figure 9c and Figure 9d. In Figure 9c, we still compare the TDVP-MU scheme and the PS scheme but with  $M = 16$ , a smaller bond dimension. Although the total error of the two schemes should be larger than the case of  $M = 64$ , their relative difference is expected to be smaller, because the reduced variational space has less numerically unoccupied states and the effect of regularization becomes negligible. Indeed, the  $\epsilon(t)$  curves of of TDVP-MU and PS are very close to each other in contrast to Figure 9b and for  $dt = 40$  the TDVP-MU scheme is even slightly more accurate than the PS scheme because TDVP-MU is free of Trotter error. To further study the impact of regularization on the accuracy, in Figure 9d, we modify the value of  $\epsilon$  in the TDVP-MU scheme and compare the results with previous ones when  $M = 64$ . We find that different



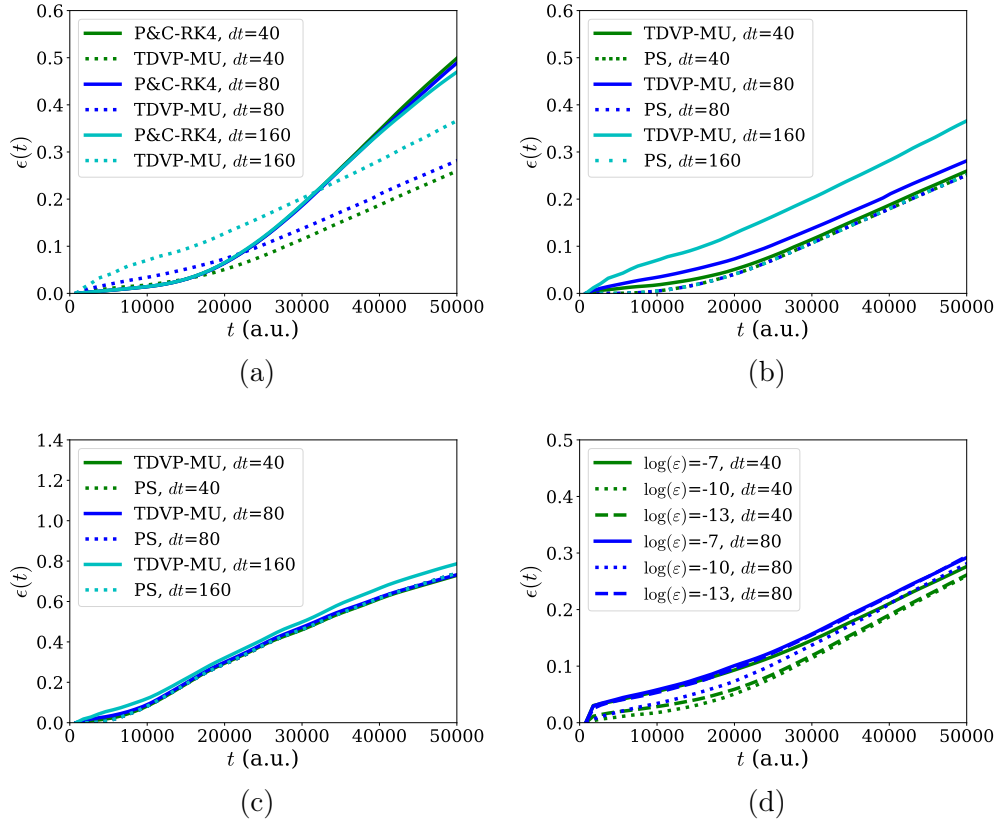


Figure 9: Direct comparison of  $\epsilon(t)$  with different schemes and parameters. (a) Comparison between P&C-RK4 and TDVP-MU. (b) and (c): Comparison between TDVP-MU and PS with  $M = 64$  and  $M = 16$  respectively. (d): Comparison of TDVP-MU with  $\epsilon = 1 \times 10^{-7}$ ,  $1 \times 10^{-10}$  and  $1 \times 10^{-13}$ .

regularization parameter will influence the short time accuracy ( $t < 5000$ ) but has little effect on the slope at long time, which has a same trend as Figure 9b. Unfortunately, Figure 9d shows that either a smaller  $\varepsilon$  or a larger  $\varepsilon$  introduces more error. Therefore adjusting the regularization parameter alone could not make TDVP-MU better. Thus we conclude that inversion instability and regularization both contribute to the error in the early stage and damage the accuracy of the TDVP-MU scheme irreversibly, which unfortunately could not be perfectly removed by striking a balance between the two.

Figure 9b also implies that a smaller  $dt$  can reduce the regularization error, thus we propose an optimized approach to carry out calculation in the TDVP-MU scheme, which is to use small steps when the evolution begins and then switch to much larger step size as the singularity of density matrix is removed. The improved accuracy is demonstrated in Figure S6.

### 3.2 Efficiency

In terms of practical application, the time costs of the algorithms should be taken into consideration when evaluating accuracy. After all, what we wish to achieve is higher accuracy with certain time, not with certain  $M$ . How hardware resource affects the computational speed is also of crucial pragmatic significance, as an inappropriate configuration could devastate efficiency as much as poorly designed algorithms or badly written code.

Although the time cost of each algorithm should vary with different implementations and there certainly are rooms for optimization in our codes, we believe the time cost presented here reflects the correct tendency. Our benchmark platforms are Intel(R) Xeon(R) CPU E5-2680 v4 @ 2.40GHz for CPU-only calculations and Intel(R) Xeon(R) Gold 5115 CPU @ 2.40GHz with NVIDIA(R) Tesla(R) V100-PCIE-32GB for CPU-GPU heterogeneous calculations. The linear algebra library we use is OPENBLAS and a comprehensive comparison between math libraries on various hardware is beyond the scope of this work.

### 3.2.1 Computational Speed of the Three Schemes on Different Hardware

To start with, we study the time cost of a single evolution step for all 3 schemes with relatively large bond dimension. The results are shown in Figure 10, with bond dimension  $M = 128$  and  $dt = 160$ . We can learn from Figure 10 that for all 3 schemes the parallel efficiency on CPU is not optimal. Using 4 cores instead of a single core can hopefully double the computational speed, however no further improvement is observed when using all 28 cores of the CPU. A more inspiring fact is that GPU is able to boost the speed of time evolution up to 33 times for TDVP based algorithms, although for the P&C-RK4 scheme the effect of GPU is not much better than 4 cores of CPU. We note that when doing calculations on GPU the GPU usage is not always 100%, so with even higher bond dimension more drastic speedup is expected. Indeed, when  $M = 256$  the time costs of the TDVP-MU scheme on single core CPU and GPU are 2580 s and 45 s respectively, indicating a 57-fold acceleration.

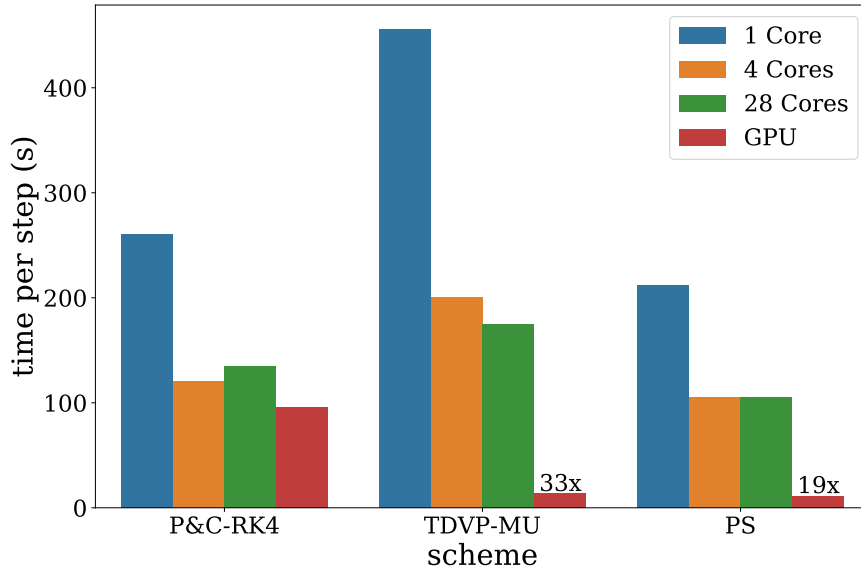


Figure 10: The time cost of each evolution step with  $M = 128$ .

On the contrary, if a smaller bond dimension is employed, devoting more resource on the computation should have less benefit. Figure 11 shows the time cost at  $M = 32$  and the

same  $dt$ . For all 3 schemes, the time cost for single core is comparable with time costs on the other hardware configurations. In particular, for TDVP based schemes the time costs with GPU are roughly the same between  $M = 128$  and  $M = 32$ , implying that in this range the latency of GPU calculation is of the same order with the actual computational time cost.

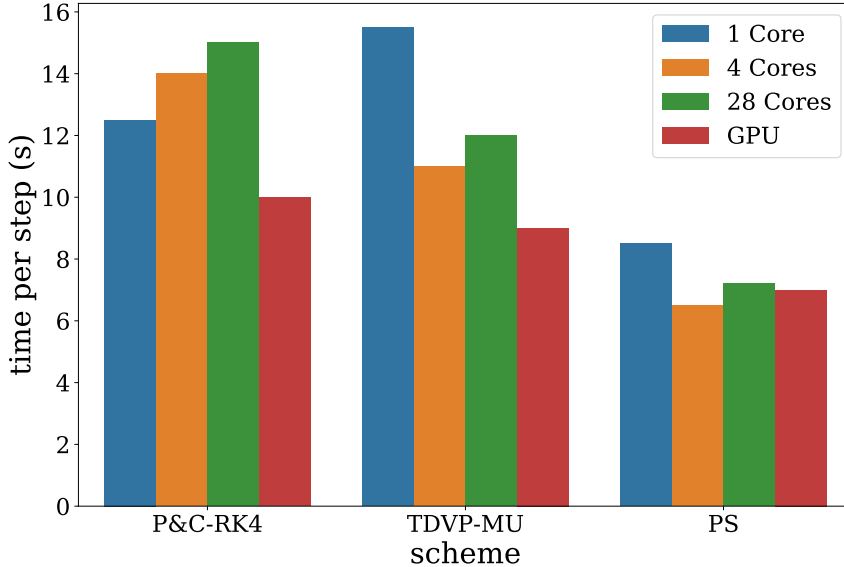


Figure 11: The time cost of each evolution step with  $M = 32$ .

To further analyze why GPU acceleration has distinct effect on P&C-RK4 scheme and TDVP based schemes, we decompose the total time cost of each evolution step into sub-steps in the evolution algorithm with  $M = 128$  and  $dt = 160$ . The numbers are obtained by sampling which function the running program is executing at uniform interval and then calculate the time used for each function according to the total time cost.

For the P&C-RK4 scheme, the bottlenecks of the algorithm are 1) QR decomposition for canonicalisation after MPO is applied on MPS and 2) Matrix multiplication to absorb coefficient matrix to the next site after QR decomposition on each site, as shown in Table 1. The two steps are both related to the necessary canonicalisation before compression and they both scale at  $\mathcal{O}(M_0^3 M_S^3 d)$ . The utilization of quantum number might help QR to run faster than matrix multiplication with single core. Note that by instinct one would expect that SVD

decomposition during the compression step would take the majority of the time, however because a compression sweep reduces bond dimension during the process, the fraction of time SVD takes is much smaller than that of QR decomposition. For single core, the time cost for SVD is 9 s including the compression after  $MPO \times MPS$  and  $MPS + MPS$  and the number remains roughly constant for other configurations. With multi-core involved, matrix multiplication costs less time, but the time cost of QR decomposition varies with a much smaller amplitude, limiting the potential of multi-core efficiency. When the calculation runs on GPU, the matrix multiplication virtually costs no time and QR decomposition becomes the sole bottleneck.

Table 1: Time cost of bottleneck sub-steps for P&C-RK4 scheme with  $M = 128$  (unit: s)

	1 core	4 cores	28 cores	GPU
Total time	260	120	135	96
QR (after $MPO \times MPS$ )	68	41	67	89
Matrix multiplication	164	50	29	< 1

For the TDVP-MU scheme, the rate determining step is the evolution of local matrix  $A_{a_{i-1}a_i}^{\sigma_i}$ , as in Table 2. The essential part of the integration is applying operators such as  $[L]_{\{a',b,a\}_{n-1}}^{(n-1)}$  and  $[R]_{\{a',b,a\}_n}^{(n)}$ , which is nothing else but matrix multiplication. Thus, the time cost of this step can be minimized by using more cores and particularly using GPU. When the algorithm runs on GPU, the SVD decomposition for regularization becomes prominent even though it only scales at  $\mathcal{O}(M_s^3 d)$ .

Table 2: Time cost of bottleneck sub-steps for TDVP-MU scheme with  $M = 128$  (unit: s)

	1 core	4 cores	28 cores	GPU
Total time	456	200	175	14
SVD	2	3	7	3
Evolve	428	183	150	8

The time cost of bottleneck sub-steps of the PS scheme are listed in Table 3, which is similar with that of TDVP-MU. A noticeable difference is that evolution of local matrix is generally faster, probably because the EOM in the PS scheme is simpler than that in the

TDVP-MU scheme and thus requires less float point operation.

Table 3: Time cost of bottleneck sub-steps for PS scheme with  $M = 128$  (unit: s)

	1 core	4 cores	28 cores	GPU
Total time	212	105	105	11
Evolve forward	143	69	59	4
QR	3	6	13	3
Evolve backward	24	11	16	3

Finally, we compare relative speed of the 3 schemes. On the one hand, if the calculation is based on CPU or the bond dimension is controlled at low level, the time consumption of the 3 methods in each step doesn't vary much regardless of the amount or architecture of computational resources. On the other hand, when carrying out CPU-GPU heterogeneous calculation and  $M$  is large, TDVP-MU scheme and PS scheme gain remarkable speed advantage over P&C-RK4 scheme owing to the efficient acceleration of matrix multiplication operations. We emphasize that in Section 3.1 we have shown the step size of the PS scheme could be dozens of times more than the step size of the other two schemes on the same accuracy level. If we wish our error is bound to  $\epsilon(\mathbf{t}) \approx 0.2$  with  $M = 128$ , then for the P&C-RK4 scheme  $dt = 160$ , for the TDVP-MU scheme  $dt = 160$  and for the PS scheme  $dt = 5760$  according to Figure 5, Figure 7 and Figure 8. Therefore, the time required for a complete simulation (till  $t = 46880$  or 1.0 ps) should be different with that of a single step. The total time required is shown in Figure 12. From the figure we can see that if step size is taken into consideration, the PS scheme is remarkably faster than the other two methods and with the aid of GPU the PS scheme is able to complete the computation within 4 minutes which is 675 times faster than the slowest single-core TDVP-MU.

### 3.2.2 Impact of Float Point Precision

Using SP instead of DP can speed all algorithms up to ideally 2 times and saves half memory, however if desired accuracy is lost then the price is too high to be acceptable. Here we compare the accuracy acquired from SP and DP computation for all 3 schemes at  $M = 128$

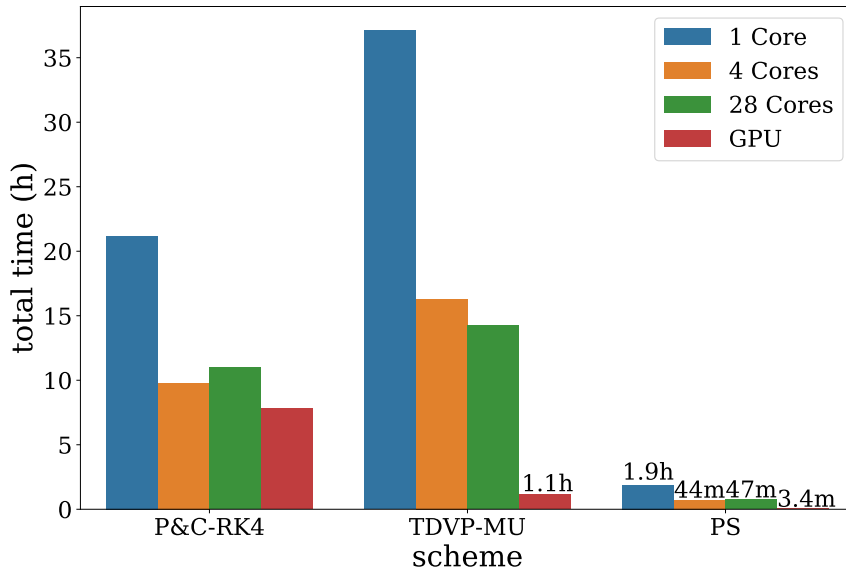


Figure 12: Total time required for a complete simulation for the 3 schemes. For the P&C-RK4 and TDVP-MU scheme  $dt = 160$  while for the PS scheme  $dt = 5760$ . The bond dimension for all three schemes is 128.

and  $dt = 160$  in Figure 13, from which we can learn that in general using SP instead of DP does not affect accuracy significantly.

We also report the increase of speed gained by using SP instead of DP in Figure 14. The benchmark is on single core CPU and similar result for GPU is shown in supporting information (Figure S8 and S9). We can see from Figure 14 that for all 3 schemes, using SP is able to double the performance because the calculation speed of almost every sub-step in the algorithms is furnished with double computational throughput. The speedup, while attractive, can be achieved by other methods, but the memory saving could be critical if the computation requires large amounts of memory.

## 4 Conclusion

To summarize, in this paper, we carry out numerical benchmark on three different TD-DMRG time evolution schemes, which are P&C-RK4, TDVP-MU and PS, in terms of ac-

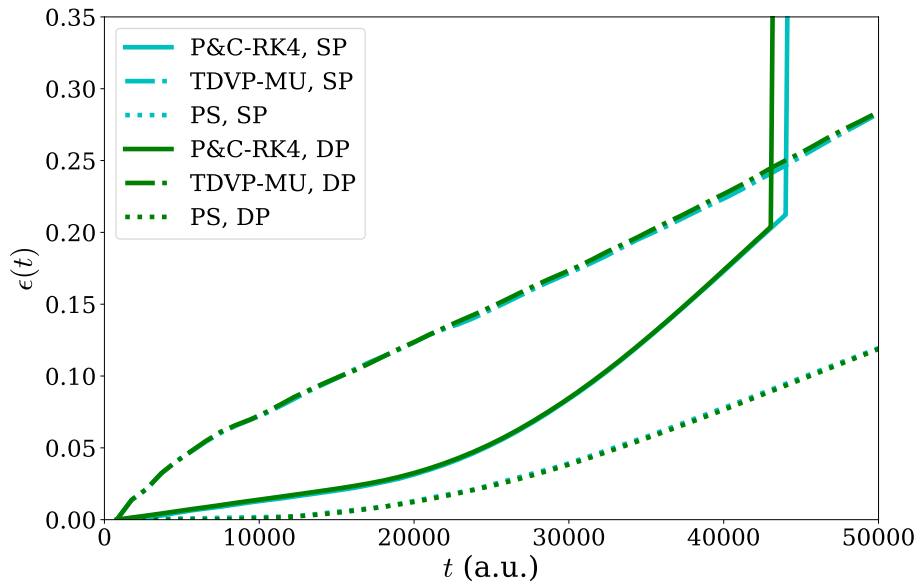


Figure 13: Accuracy of the 3 schemes with  $M = 128$  and  $dt = 160$  in SP and DP respectively.

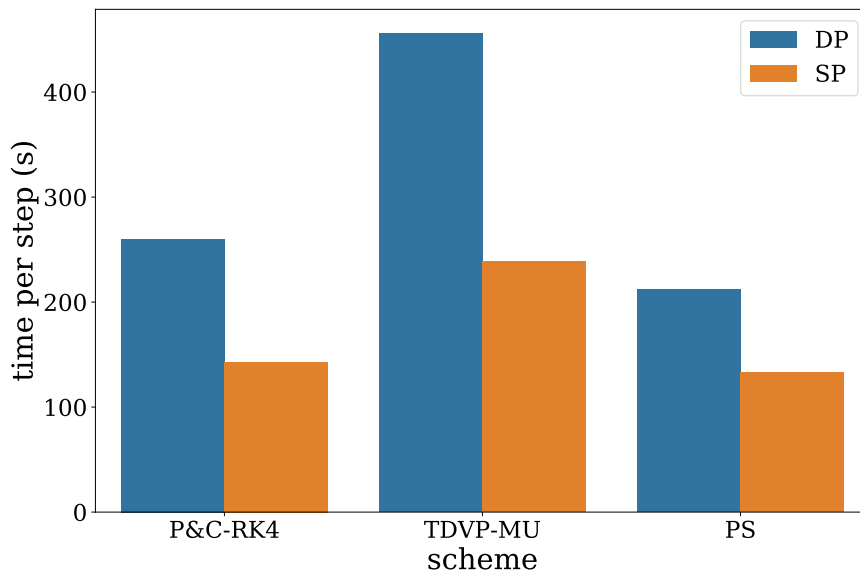


Figure 14: The time cost of each evolution step in DP and SP for the 3 schemes on single core CPU.



curacy and speed. It is found that among the three schemes PS is in general the most accurate and allows the largest time step, because the propagation process is unitary and free of regularization. The P&C-RK4 scheme performs well when the total evolution time is short, however the error accumulates much faster and becomes the largest among the three schemes in the long term. Furthermore, it is not worthwhile to change the compression strategy from fixing the bond dimension  $M$  to fixing the singular value truncation threshold  $\zeta$ . The TDVP-MU scheme could reach the same accuracy as the PS scheme with small bond dimension  $M$  and time step  $dt$ , since both of them are based on TDVP. However, when increasing  $M$  and  $dt$ , TDVP-MU is less accurate than PS because of the unavoidable error in the matrix inversion and regularization. Regarding efficiency, we conclude that the PS scheme is remarkably the fastest due to the fact that although the time required for each step is of the same magnitude on CPUs, the step size of the PS scheme is 36 times larger than the other two schemes in our case. Moreover, GPUs are able to speed up TDVP-MU and PS for up to 57 times due to the efficient acceleration of tensor contraction. We find that in order to simulate dynamics of the 252-DOF 7-site FMO model to 1 ps at relatively high accuracy, while the worst strategy takes more than 36 hours to complete the calculation, the best strategy which is to use the largest time step in the PS scheme with GPU acceleration is able to finish within 4 minutes. We also conclude that using single precision float number does not change the accuracy of time evolution significantly in the FMO model. However, we notice in some preliminary tests that in imaginary time propagation some of the rules above does not apply including the interchangeability of SP and DP float numbers and related research on this topic is underway. Our work provides benchmarks of the three evolution schemes and serves as a reference for researchers to choose optimal computational hardware for their TD-DMRG calculation.

## Acknowledgement

This work is supported by the National Natural Science Foundation of China through the project “Science Center for Luminescence from Molecular Aggregates (SCELMA)” Grant Number 21788102, as well as by the Ministry of Science and Technology of China through the National Key R&D Plan Grant Number 2017YFA0204501. The authors are indebted to Prof. Garnet Chan for the stimulating discussions. The authors gratefully thank Mr. Hongde Yu for support on crystal structure of the FMO complex.

## Supporting Information Available

The following files are available free of charge.

- Filename: SI.pdf

$\epsilon(t)$  for all parameters, results at finite temperature, evidence of RK4 error in the P&C-RK4 scheme, optimized TDVP-MU evolution strategy, populations dynamics with large  $dt$  in the PS scheme, SP acceleration and memory consumption on GPU.

This information is available free of charge via the Internet at <http://pubs.acs.org>

## References

- (1) Ma, H.; Luo, Z.; Yao, Y. The time-dependent density matrix renormalisation group method. *Mol. Phys.* **2018**, *116*, 854–868.
- (2) Paeckel, S.; Köhler, T.; Swoboda, A.; Manmana, S. R.; Schollwöck, U.; Hubig, C. Time-evolution methods for matrix-product states. *arXiv preprint arXiv:1901.05824* **2019**,
- (3) White, S. R. Density Matrix Formulation for Quantum Renormalization Groups. *Phys. Rev. Lett.* **1992**, *69*, 2863.

- (4) White, S. R. Density-matrix Algorithms for Quantum Renormalization Groups. *Phys. Rev. B* **1993**, *48*, 10345.
- (5) Shuai, Z.; Brédas, J. L.; Saxena, A.; Bishop, A. R. Linear and nonlinear optical response of polyenes: A density matrix renormalization group study. *J. Chem. Phys.* **1998**, *109*, 2549–2555.
- (6) Zhang, C.; Jeckelmann, E.; White, S. R. Dynamical properties of the one-dimensional Holstein model. *Phys. Rev. B* **1999**, *60*, 14092.
- (7) Yao, Y. Polaronic quantum diffusion in dynamic localization regime. *New J. Phys.* **2017**, *19*, 043015.
- (8) Barford, W.; Mannouch, J. R. Torsionally induced exciton localization and decoherence in  $\pi$ -conjugated polymers. *J. Chem. Phys.* **2018**, *149*, 214107.
- (9) Greene, S. M.; Batista, V. S. Tensor-Train Split-Operator Fourier Transform (TT-SOFT) Method: Multidimensional Nonadiabatic Quantum Dynamics. *J. Chem. Theory Comput.* **2017**, *13*, 4034–4042, PMID: 28763215.
- (10) Baiardi, A.; Reiher, M. Large-scale quantum-dynamics with matrix product states. *J. Chem. Theory Comput.* **2019**,
- (11) Ronca, E.; Li, Z.; Jimenez-Hoyos, C. A.; Chan, G. K.-L. Time-Step Targeting Time-Dependent and Dynamical Density Matrix Renormalization Group Algorithms with ab Initio Hamiltonians. *J. Chem. Theory Comput.* **2017**, *13*, 5560–5571, PMID: 28953377.
- (12) Yao, Y.; Sun, K.-W.; Luo, Z.; Ma, H. Full Quantum Dynamics Simulation of a Realistic Molecular System Using the Adaptive Time-Dependent Density Matrix Renormalization Group Method. *J. Phys. Chem. Lett.* **2018**, *9*, 413–419, PMID: 29298068.
- (13) Ren, J.; Shuai, Z.; Chan, G. K. Time-Dependent Density Matrix Renormalization Group Algorithms for Nearly Exact Absorption and Fluorescence Spectra of Molecular

- Aggregates at Both Zero and Finite Temperature. *J. Chem. Theory Comput.* **2018**, *14*, 5027–5039.
- (14) Cai, Z.; Barthel, T. Algebraic versus Exponential Decoherence in Dissipative Many-Particle Systems. *Phys. Rev. Lett.* **2013**, *111*, 150403.
- (15) W. Chin, A.; Prior, J.; Rosenbach, R.; Caycedo-Soler, F.; Huelga, S.; Plenio, M. The role of non-equilibrium vibrational structures in electronic coherence and recoherence in pigment-protein complexes. *Nat. Phys.* **2013**, *9*, 113–118.
- (16) Borrelli, R.; F. Gelin, M. Simulation of Quantum Dynamics of Excitonic Systems at Finite Temperature: An efficient method based on Thermo Field Dynamics. *Sci. Rep.* **2017**, *7*, 9127.
- (17) A. Y. N. Schröder, F.; H. P. Turban, D.; Musser, A.; Hine, N.; W. Chin, A. Tensor network simulation of multi-environmental open quantum dynamics via machine learning and entanglement renormalisation. *Nat. Commun.* **2019**, *10*, 1062.
- (18) Kloss, B.; Bar Lev, Y. Spin transport in a long-range-interacting spin chain. *Phys. Rev. A* **2019**, *99*, 032114.
- (19) Frahm, L.-H.; Pfannkuche, D. Ultrafast ab Initio Quantum Chemistry Using Matrix Product States. *J. Chem. Theory Comput.* **2019**, *15*, 2154–2165.
- (20) Vidal, G. Efficient simulation of one-dimensional quantum many-body systems. *Phys. Rev. Lett.* **2004**, *93*, 040502.
- (21) White, S. R.; Feiguin, A. E. Real-time evolution using the density matrix renormalization group. *Phys. Rev. Lett.* **2004**, *93*, 076401.
- (22) Daley, A. J.; Kollath, C.; Schollwöck, U.; Vidal, G. Time-dependent density-matrix renormalization-group using adaptive effective Hilbert spaces. *J. Stat. Mech.: Theory Exp.* **2004**, *2004*, P04005.

- (23) Zaletel, M. P.; Mong, R. S.; Karrasch, C.; Moore, J. E.; Pollmann, F. Time-evolving a matrix product state with long-ranged interactions. *Phys. Rev. B* **2015**, *91*, 165112.
- (24) García-Ripoll, J. J. Time evolution of Matrix Product States. *New J. Phys.* **2006**, *8*, 305–305.
- (25) Halimeh, J. C.; Kolley, F.; McCulloch, I. P. Chebyshev matrix product state approach for time evolution. *Phys. Rev. B* **2015**, *92*, 115130.
- (26) Wall, M. L.; Carr, L. D. Out-of-equilibrium dynamics with matrix product states. *New J. Phys.* **2012**, *14*, 125015.
- (27) Feiguin, A. E.; White, S. R. Time-step targeting methods for real-time dynamics using the density matrix renormalization group. *Phys. Rev. B* **2005**, *72*, 020404.
- (28) Dutta, T.; Ramasesha, S. Double time window targeting technique: Real-time DMRG dynamics in the Pariser-Parr-Pople model. *Phys. Rev. B* **2010**, *82*, 035115.
- (29) Dirac, P. A. M. Note on Exchange Phenomena in the Thomas Atom. *Math. Proc. Camb. Philos. Soc.* **1930**, *26*, 376–385.
- (30) Langhoff, P. W.; Epstein, S. T.; Karplus, M. Aspects of Time-Dependent Perturbation Theory. *Rev. Mod. Phys.* **1972**, *44*, 602–644.
- (31) Haegeman, J.; Cirac, J. I.; Osborne, T. J.; Pižorn, I.; Verschelde, H.; Verstraete, F. Time-dependent variational principle for quantum lattices. *Phys. Rev. Lett.* **2011**, *107*, 070601.
- (32) Haegeman, J.; Lubich, C.; Oseledets, I.; Vandereycken, B.; Verstraete, F. Unifying time evolution and optimization with matrix product states. *Phys. Rev. B* **2016**, *94*, 165116.
- (33) Meyer, H.-D.; Manthe, U.; Cederbaum, L. The multi-configurational time-dependent Hartree approach. *Chem. Phys. Lett.* **1990**, *165*, 73 – 78.

- (34) Wang, H.; Thoss, M. Multilayer formulation of the multiconfiguration time-dependent Hartree theory. *J. Chem. Phys.* **2003**, *119*, 1289–1299.
- (35) Beck, M. H.; Jäckle, A.; Worth, G. A.; Meyer, H.-D. The multiconfiguration time-dependent Hartree (MCTDH) method: a highly efficient algorithm for propagating wavepackets. *Phys. Rep.* **2000**, *324*, 1–105.
- (36) Kloss, B.; Burghardt, I.; Lubich, C. Implementation of a novel projector-splitting integrator for the multi-configurational time-dependent Hartree approach. *J. Chem. Phys.* **2017**, *146*, 174107.
- (37) Bonfanti, M.; Burghardt, I. Tangent space formulation of the Multi-Configuration Time-Dependent Hartree equations of motion: The projector-splitting algorithm revisited. *Chem. Phys.* **2018**, *515*, 252–261.
- (38) Kurashige, Y. Matrix product state formulation of the multiconfiguration time-dependent Hartree theory. *J. Chem. Phys.* **2018**, *149*, 194114.
- (39) Hauschild, J.; Pollmann, F. Efficient numerical simulations with Tensor Networks: Tensor Network Python (TeNPy). *SciPost Phys. Lect. Notes* **2018**, *5*, Code available from <https://github.com/tenpy/tenpy>.
- (40) Mendl, C. B. PyTeNet: A concise Python implementation of quantum tensor network algorithms. *J. Open Source Softw.* **2018**, *3*, 948.
- (41) Ufimtsev, I. S.; Martinez, T. J. Quantum chemistry on graphical processing units. 1. Strategies for two-electron integral evaluation. *J. Chem. Theory Comput.* **2008**, *4*, 222–231.
- (42) Ufimtsev, I. S.; Martinez, T. J. Quantum Chemistry on Graphical Processing Units. 2. Direct Self-Consistent-Field Implementation. *J. Chem. Theory Comput.* **2009**, *5*, 1004–1015.

- (43) Shee, J.; Arthur, E. J.; Zhang, S.; Reichman, D. R.; Friesner, R. A. Phaseless Auxiliary-Field Quantum Monte Carlo on Graphical Processing Units. *J. Chem. theory Comput.* **2018**, *14*, 4109–4121.
- (44) Harvey, M. J.; Giupponi, G.; De Fabritiis, G. ACEMD: Accelerating Biomolecular Dynamics in the Microsecond Time Scale. *J. Chem. Theory Comput.* **2009**, *5*, 1632–1639.
- (45) Ufimtsev, I. S.; Martinez, T. J. Quantum Chemistry on Graphical Processing Units. 3. Analytical Energy Gradients, Geometry Optimization, and First Principles Molecular Dynamics. *J. Chem. Theory Comput.* **2009**, *5*, 2619–2628.
- (46) Penfold, T. Accelerating direct quantum dynamics using graphical processing units. *Phys. Chem. Chem. Phys.* **2017**, *19*, 19601–19608.
- (47) Kreisbeck, C.; Kramer, T.; Rodríguez, M.; Hein, B. High-performance solution of hierarchical equations of motion for studying energy transfer in light-harvesting complexes. *J. Chem. Theory Comput.* **2011**, *7*, 2166–2174.
- (48) Tsuchimoto, M.; Tanimura, Y. Spins dynamics in a dissipative environment: hierarchical equations of motion approach using a Graphics Processing Unit (GPU). *J. Chem. Theory Comput.* **2015**, *11*, 3859–3865.
- (49) Yu, J.; Hsiao, H.-C.; Kao, Y.-J. GPU accelerated tensor contractions in the plaquette renormalization scheme. *Comput. Fluids* **2011**, *45*, 55 – 58, 22nd International Conference on Parallel Computational Fluid Dynamics (ParCFD 2010).
- (50) Nemes, C.; Barcza, G.; Nagy, Z.; Örs Legeza,; Szolgay, P. The density matrix renormalization group algorithm on kilo-processor architectures: Implementation and trade-offs. *Comput. Phys. Commun.* **2014**, *185*, 1570 – 1581.

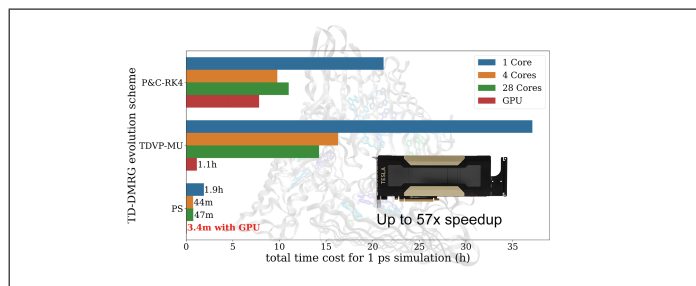
- (51) Luehr, N.; Ufimtsev, I. S.; Martínez, T. J. Dynamic Precision for Electron Repulsion Integral Evaluation on Graphical Processing Units (GPUs). *J. Chem. Theory Comput.* **2011**, *7*, 949–954, PMID: 26606344.
- (52) Grand, S. L.; Götz, A. W.; Walker, R. C. SPFP: Speed without compromise—A mixed precision model for GPU accelerated molecular dynamics simulations. *Comput. Phys. Commun.* **2013**, *184*, 374 – 380.
- (53) Pokhilko, P.; Epifanovsky, E.; Krylov, A. I. Double Precision Is Not Needed for Many-Body Calculations: Emergent Conventional Wisdom. *J. Chem. Theory Comput.* **2018**, *14*, 4088–4096, PMID: 29969560.
- (54) S Engel, G.; R Calhoun, T.; Read, E.; Ahn, T.-K.; Mancal, T.; Cheng, Y.-C.; Blankenship, R.; R Fleming, G. Evidence for wavelike energy transfer through quantum coherence in photosynthetic systems. *Nature* **2007**, *446*, 782–6.
- (55) Mohseni, M.; Rebentrost, P.; Lloyd, S.; Aspuru-Guzik, A. Environment-assisted quantum walks in photosynthetic energy transfer. *J. Chem. Phys.* **2008**, *129*, 174106.
- (56) Nalbach, P.; Braun, D.; Thorwart, M. Exciton transfer dynamics and quantumness of energy transfer in the Fenna-Matthews-Olson complex. *Phys. Rev. E* **2011**, *84*, 041926.
- (57) Ishizaki, A.; Fleming, G. R. Theoretical examination of quantum coherence in a photosynthetic system at physiological temperature. *Proc. Natl. Acad. Sci. U. S. A.* **2009**, *106*, 17255–17260.
- (58) Wilkins, D. M.; Dattani, N. S. Why Quantum Coherence Is Not Important in the Fenna–Matthews–Olsen Complex. *J. Chem. Theory Comput.* **2015**, *11*, 3411–3419, PMID: 26575775.
- (59) Schulze, J.; Kühn, O. Explicit Correlated Exciton-Vibrational Dynamics of the FMO Complex. *J. Phys. Chem. B* **2015**, *119*, 6211–6216, PMID: 25927682.



- (60) Schulze, J.; Shibl, M. F.; Al-Marri, M. J.; Kühn, O. Multi-layer multi-configuration time-dependent Hartree (ML-MCTDH) approach to the correlated exciton-vibrational dynamics in the FMO complex. *J. Chem. Phys.* **2016**, *144*, 185101.
- (61) Schollwöck, U. The density-matrix renormalization group in the age of matrix product states. *Ann. Phys.* **2011**, *326*, 96–192.
- (62) Chan, G. K.-L.; Keselman, A.; Nakatani, N.; Li, Z.; White, S. R. Matrix product operators, matrix product states, and ab initio density matrix renormalization group algorithms. *J. Chem. Phys.* **2016**, *145*, 014102.
- (63) Meyer, H.-D.; Wang, H. On regularizing the MCTDH equations of motion. *J. Chem. Phys.* **2018**, *148*, 124105.
- (64) Wang, H.; Meyer, H.-D. On regularizing the ML-MCTDH equations of motion. *J. Chem. Phys.* **2018**, *149*, 044119.
- (65) Lubich, C.; Oseledets, I.; Vandereycken, B. Time Integration of Tensor Trains. *SIAM J. Numer. Anal.* **2015**, *53*, 917–941.
- (66) Lubich, C.; Rohwedder, T.; Schneider, R.; Vandereycken, B. Dynamical approximation by hierarchical Tucker and tensor-train tensors. *SIAM J. Matrix Anal. Appl.* **2013**, *34*, 470–494.
- (67) Hochbruck, M.; Lubich, C. On Krylov Subspace Approximations to the Matrix Exponential Operator. *SIAM J. Numer. Anal.* **1997**, *34*, 1911–1925.
- (68) Chan, G. K.-L. An algorithm for large scale density matrix renormalization group calculations. *J. Chem. Phys.* **2004**, *120*, 3172–3178.
- (69) Kurashige, Y.; Yanai, T. High-performance ab initio density matrix renormalization group method: Applicability to large-scale multireference problems for metal compounds. *J. Chem. Phys.* **2009**, *130*, 234114.

- (70) Stoudenmire, E. M.; White, S. R. Real-space parallel density matrix renormalization group. *Phys. Rev. B* **2013**, *87*, 155137.
- (71) Holstein, T. Studies of polaron motion: Part I. The molecular-crystal model. *Ann. Phys.* **1959**, *8*, 325–342.
- (72) Schröter, M.; Ivanov, S.; Schulze, J.; Polyutov, S.; Yan, Y.; Pullerits, T.; Kühn, O. Exciton–vibrational coupling in the dynamics and spectroscopy of Frenkel excitons in molecular aggregates. *Phys. Rep.* **2015**, *567*, 1–78.
- (73) Tronrud, D. E.; Wen, J.; Gay, L.; Blankenship, R. E. The structural basis for the difference in absorbance spectra for the FMO antenna protein from various green sulfur bacteria. *Photosynth. Res.* **2009**, *100*, 79–87.
- (74) Moix, J.; Wu, J.; Huo, P.; Coker, D.; Cao, J. Efficient Energy Transfer in Light-Harvesting Systems, III: The Influence of the Eighth Bacteriochlorophyll on the Dynamics and Efficiency in FMO. *J. Phys. Chem. Lett.* **2011**, *2*, 3045–3052.
- (75) Wendling, M.; Pullerits, T.; A. Przyjalowski, M.; I. E. Vulto, S.; Aartsma, T.; van Grondelle, R.; Van Amerongen, H. Electron-Vibrational Coupling in the Fenna-Matthews-Olson Complex of *Prosthecochloris a estuarii* Determined by Temperature-Dependent Absorption and Fluorescence Line-Narrowing Measurements. *J. Phys. Chem. B* **2000**, *104*, 5825–5831.
- (76) Nielsen, M. A.; Chuang, I. L. *Quantum Computation and Quantum Information*; Cambridge University Press, 2000.
- (77) Feiguin, A. E.; White, S. R. Finite-temperature density matrix renormalization using an enlarged Hilbert space. *Phys. Rev. B* **2005**, *72*, 220401.

# Graphical TOC Entry



Supporting information for:  
Numerical Assessment for Accuracy and  
Efficiency of Time Evolution Schemes in  
TD-DMRG algorithm: CPU vs GPU

Weitang Li, Jiajun Ren,<sup>\*</sup> and Zhigang Shuai

*MOE Key Laboratory of Organic OptoElectronics and Molecular Engineering, Department  
of Chemistry, Tsinghua University, Beijing 100084, People's Republic of China*

E-mail: renjj@mail.tsinghua.edu.cn

### $\epsilon(t)$ for All Parameters

In the main text we only present a subset of our results to demonstrate our points, here we provide  $\epsilon(t)$  for all 3 schemes at a broad range of  $M$  and  $dt$  in Figure S1. For the TDVP-MU scheme, when  $320 < dt$  we observe a dramatic increase of  $\epsilon(t)$  which is not discussed in the main text. We believe the reason for the phenomenon is that the large error introduced at the early stage of the evolution is too large to be “self-healed” as discussed in MCTDH literature.<sup>?</sup>

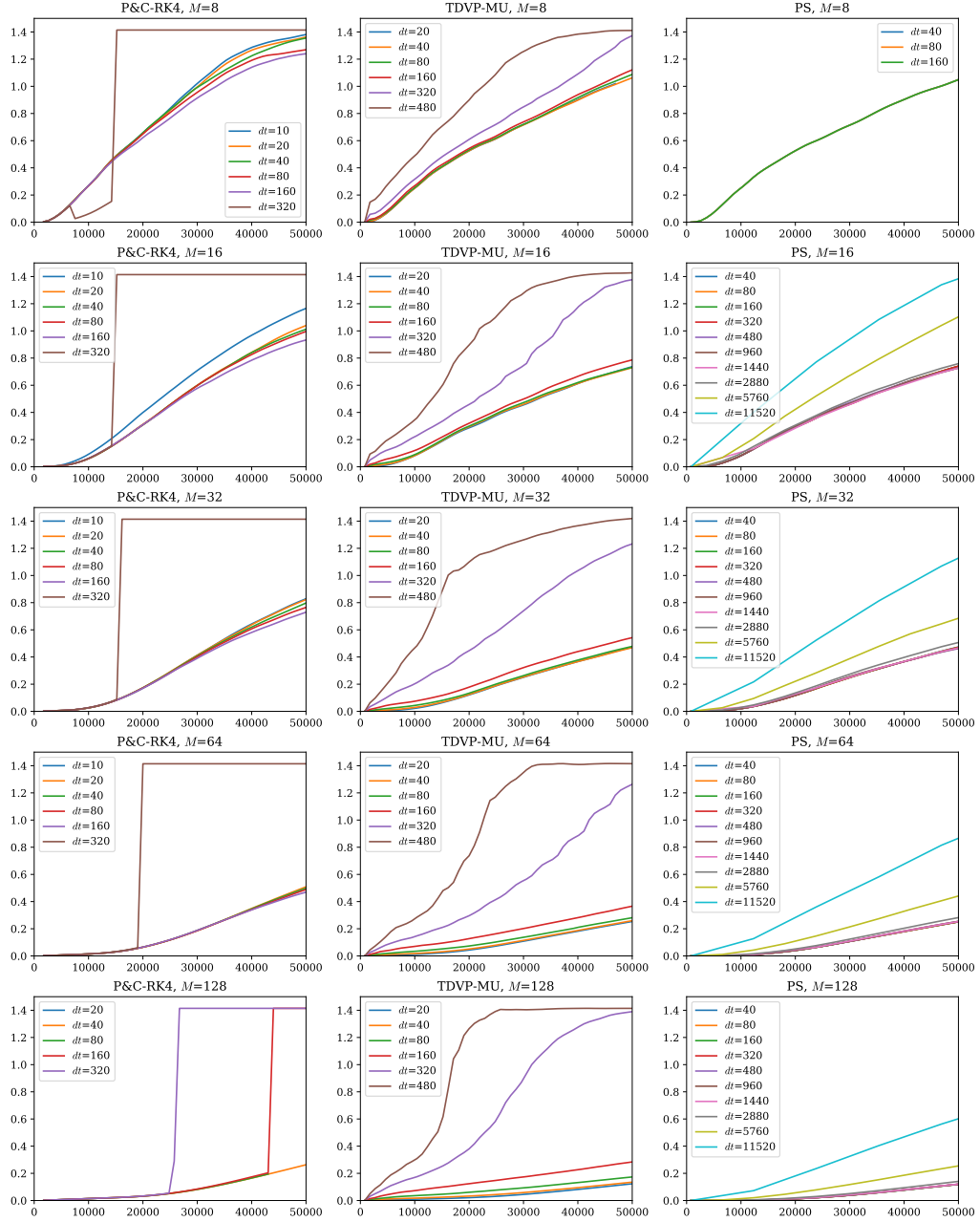


Figure S1:  $\epsilon(t)$  for the 3 schemes at  $M = 8, 16, 32, 64, 128$ .

# Results at Finite Temperature

$\epsilon(t)$  obtained at finite temperature (77 K) is presented in Figure S2, Figure S3 and Figure S4. The initial thermal states are obtained analytically. The maximum bond dimension employed in the calculations is 64 because higher bond dimension would require more than 128 GigaBytes (GB) of memory during the initial P&C-RK4 which is beyond our computing capability. The population dynamics can not converge with  $M \leq 64$ . The fact is easy to understand because in zero temperature we need  $M = 256$  and finite temperature calculation should require larger bond dimension. Limited by the small bond dimension, the errors are large in all 3 schemes and we consider certain subtle results to be unreliable. However, it's still safe to say that the PS is the most accurate scheme.

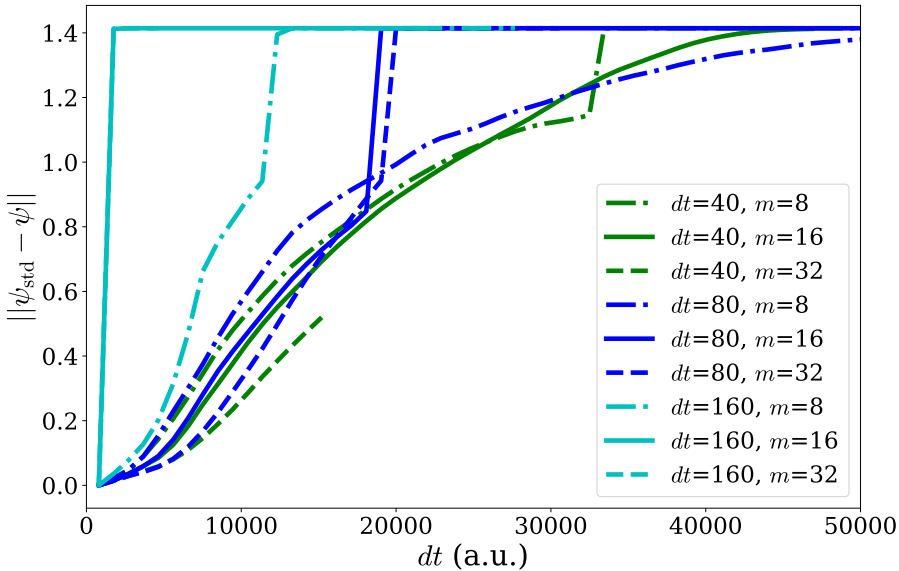


Figure S2:  $\epsilon(t)$  for the P&C-RK4 scheme at finite temperature.

## Evidence of RK4 Error in the P&C-RK4 Scheme

Theoretically in the P&C-RK4 scheme relatively large  $dt$  causes the RK4 propagator to produce more error thus there should be a region where  $\epsilon(t)$  is positively correlated with  $dt$ .

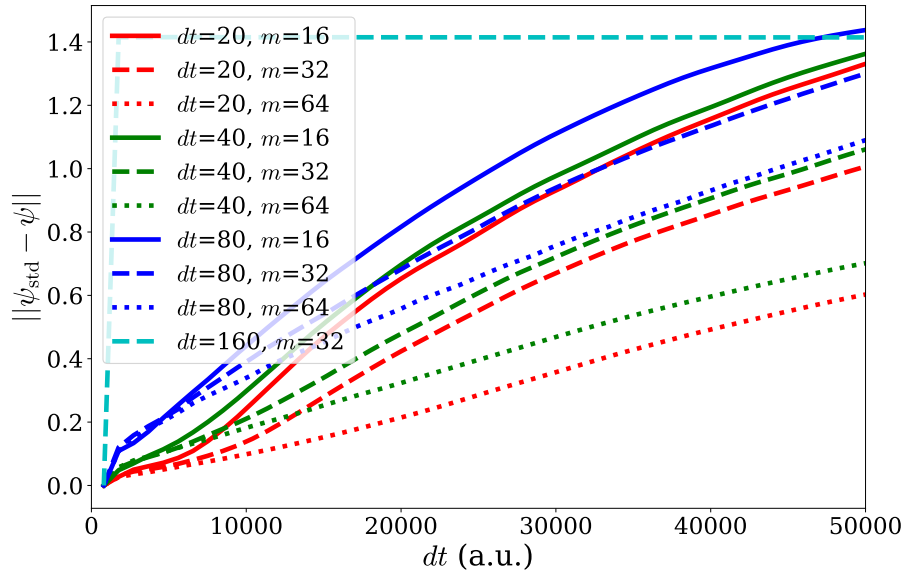


Figure S3:  $\epsilon(t)$  for the TDVP-MU scheme at finite temperature.

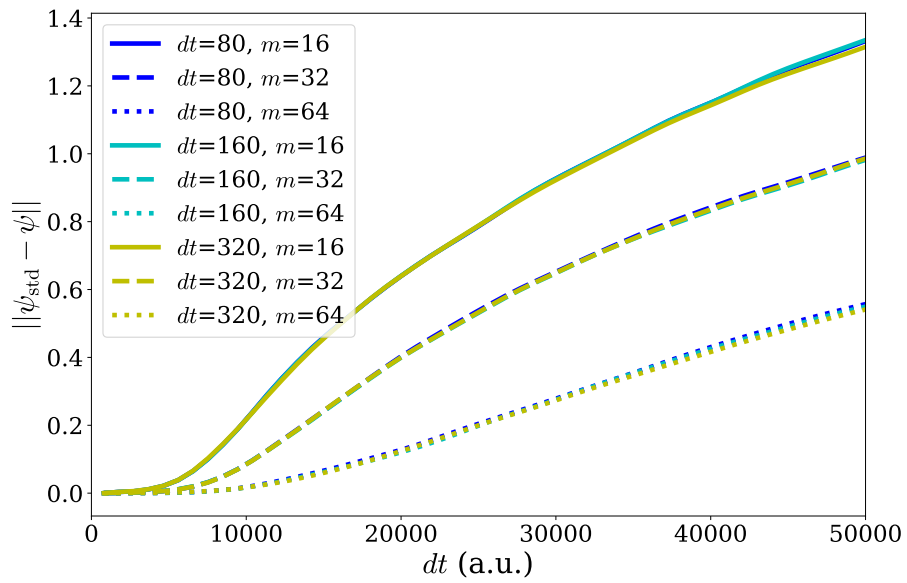


Figure S4:  $\epsilon(t)$  for the PS scheme at finite temperature.

Such region is not shown in the main text because of the dominance of truncation error at long time scale. Here we present evidence of the RK4 error when  $\mathbf{t}' = 3680$  in Figure S5. At the early stage of the simulation the entanglement of the state is not strong and the error introduced by truncation is smaller than the RK4 error.

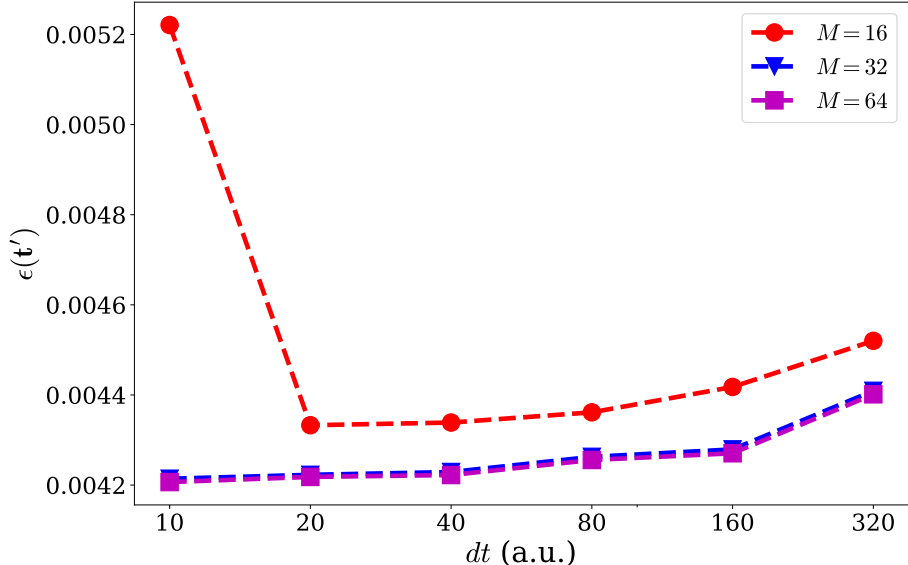


Figure S5:  $\epsilon(\mathbf{t}')$  for the P&C-RK4 scheme where  $\mathbf{t}' = 3680$ .

## Optimized TDVP-MU Evolution Strategy

In the main text we mentioned that for the TDVP-MU scheme an optimal strategy to carry out time evolution is to use small  $dt$  at early stages to reduce the error caused by inversion instability and regularization. For simplicity, we denote the method as “adaptive TDVP-MU”. Here we present results obtained by adaptive TDVP-MU in Figure S6. We use  $dt$  based on Table S1.

We can learn from Figure S6 that the overall result is significantly better than the TDVP-MU scheme with  $dt = 160$ , however initially we expect the result to be as precise as PS with  $dt = 160$  which is not achieved. The reason for this is still under investigation.



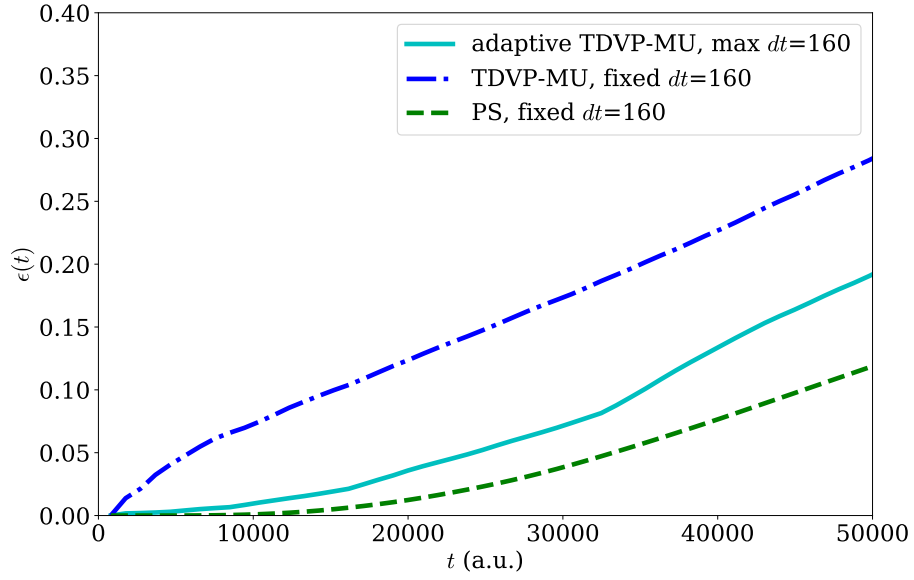


Figure S6: Effect of the optimized TDVP-MU time evolution strategy (adaptive TDVP-MU).

Table S1:  $dt$  used during time evolution of adaptive TDVP-MU

$t$	$dt$
800-2800	5
2800-4800	10
4800-8800	20
8800-16800	40
16800-32800	80
32800-	160

## Populations Dynamics with Large $dt$ in the PS Scheme

The extraordinary large  $dt$  in the PS scheme is suspicious at first glance, so we double-checked the population dynamics obtained with such large  $dt$  in Figure S7. Although the “resolution” of the curves is low due to the large  $dt$  and certain fine structures in the curves are smeared out, the expectation values of physical observables such as exciton populations are still accurate and the result is reliable if we are only interested in the last state of the simulation.

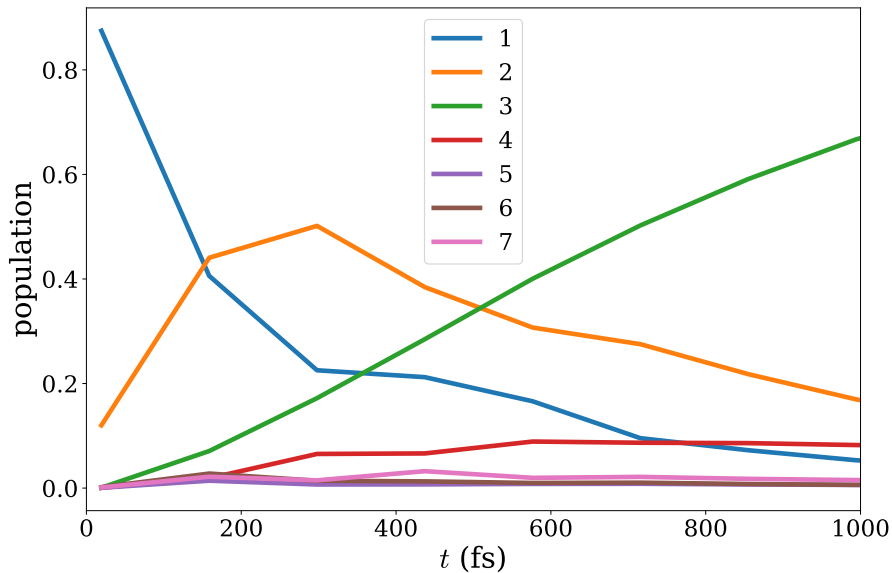


Figure S7: Population dynamics obtained by the PS scheme with  $M = 128$  and  $dt = 5760$ .

## SP Acceleration on GPU

Theoretically, using SP on GPU is able to double the computational speed, however, on GPU such effect is not prominent with  $M = 128$  due to GPU latency (Figure S8). We expect at higher bond dimension SP should have more advantage over DP and the result is shown in Figure S9.

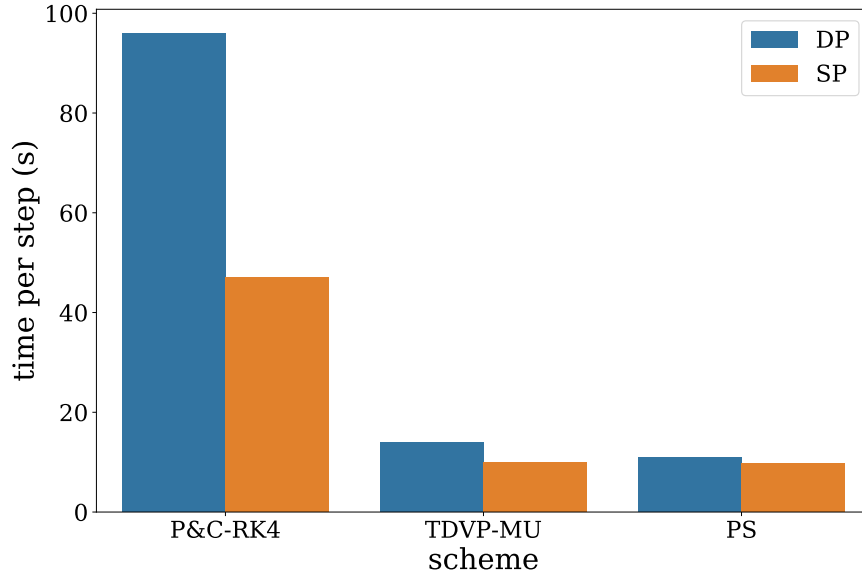


Figure S8: The time cost of each evolution step in DP and SP for the 3 schemes on GPU with  $M = 128$ .

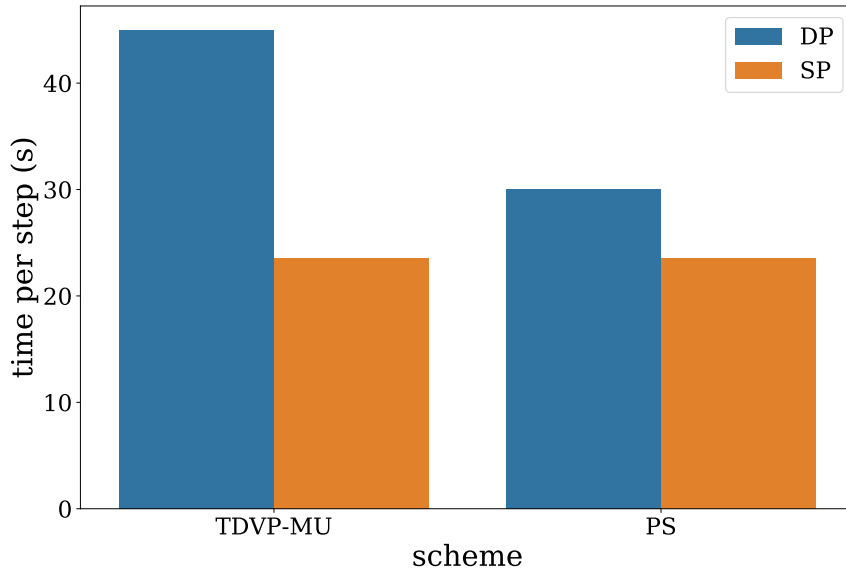


Figure S9: The time cost of each evolution step in DP and SP for TDVP-MU scheme and PS scheme on GPU with  $M = 256$ .

# Memory Consumption on GPU

We note that memory consumption is usually a bottleneck for GPU computation. According to our experience the memory scheduler in the library we use<sup>?</sup> takes 2 to 5 times of the actually memory needed to accelerate memory allocation. If the memory scheduler is disabled, the overhead caused by memory allocation would reduce the computational speed by more than 70%. The memory usage we observed in our calculation is shown in Table S2.

As the total memory of our GPU is 32 GB, we can not measure memory usage above this threshold as in the case of  $M = 256$  in the P&C-RK4 scheme. The reason why the P&C-RK4 scheme demands significantly larger memory is that in this scheme the intermediate MPS created by MPO applying on MPS must be stored in complete form which could be a hundred times larger than the original MPS.

Table S2: The memory table (Unit: GB)

$M$	P&C-RK4	TDVP-MU	PS
64	4.7	6.0	1.1
128	15.7	3.8	2.8
256	>32	11.2	8.8